Thin-Film Gated Photocathodes for Multiple-Beam Electron-Beam Lithography

Zeting Pei

B.S. in Materials Science and Engineering,
Central-South University of Technology, China, 1989
M.S. in Materials Science and Engineering,
Oregon Graduate Institute of Science and Technology, 1998

A dissertation presented to the faculty of the
Oregon Graduate Institute of Science and Technology
in partial fulfillment of the
requirements for the degree
Doctor of Philosophy
in
Electrical Engineering

February 2001

The dissertation “Thin-Film Grated Photocathodes for Multiple-Beam Electron-Beam Lithography” by Zeting Pei has been examined and approved by the following Examination Committee:

Dr. C. Neil Berglund, Advisor
Professor

Dr. Jack McCarthy
Assistant Professor

Dr. Rajendra Solanki
Professor

Dr. Mark Gesley
Etec Systems, Inc.

To

My mother & my wife

Acknowledgements

On completion of my graduate study, I would like to express my great thanks and my gratitude to my supervisor, Dr. C. Neil Berglund for his intelligent guidance, earnest stimulation, and enthusiastic encouragement. The examples are so extensive that I could not list all of them here. But the most impressive and valuable education I have accepted so far is that Dr. Berglund repeatedly taught me how to define a problem first and then deal with it. I gratefully acknowledge the success of this thesis research ascribed to this training, and I am sure that I will continuously benefit from this education in my professional carrier.

Special thanks to Etec Systems, Inc. and DARPA for funding this project. I was also inspired by the technology advances in Etec and by the knowledgeable people there.

I wish to thank the members of thesis committee, Dr. Jack McCarthy, Dr. Raj Solanki and Dr. Mark Gesley for reviewing this thesis and for their suggestions. I am very grateful for Dr. McCarthy's help on the sample fabrication and on using equipment in his lab.

I am greatly indebted to Dr. Jody L. House for her editing this thesis and for her constructive criticisms.

My thanks also extend to Dr. Xiaolan Chen, Dr. Suresh Gosavi and Mr. Tim Thomas, for their help in the initial phase of this research.

I am grateful to Mr. & Ms Richard and Susan McElroy for their generosity, help and friendship in the past four years.

Finally, my special thanks to my wife Yuebo Liu for her endless love, patience and support.

Table of Contents

List of tables

List of figures

List of symbols

A	area
A**	Richardson constant, 1.2×10^6 amp/meter^2 kelvin^2
B	electron-beam brightness
C_c	chromatic aberration coefficient
C_s	spherical aberration coefficient
E	electron energy
E_2	accelerating field
E_{max}	maximum electron energy of photoemission
F(E,x)	fraction of electron
$H(\phi)$	angular distribution function
$H_i(\phi)$	angular distribution function of an individual electron energy level
I	current
I_0	current of a probe in normal direction
I_a	anode current
I_b	electron-beam current
I_c	cathode current
I_g	gate current
I_p	absorbed light
I_{p0}	incident light
J	current density
J_0	current density of a probe in normal direction
J'	normalized current density
L(E)	electron-electron scattering length
M	column demagnification

N_V	valence-band optical density of state
N_C	conduction-band optical density of state
P	probability
P_i	incident optical power
Q	charge dose
QE	quantum efficiency
QY	quantum yield
R	reflectivity
T	temperature
V	voltage
V_b	electron beam voltage
V_g	gate voltage
V_R	retarding potential
V_x	extinction gate voltage
d	gate diameter
d_0	beam diameter at crossover
d_c	electron-beam diameter due to chromatic aberration
d_d	electron-beam diameter due to diffraction
d_g	demagnified electron-beam diameter
d_s	electron-beam diameter due to spherical aberration
d_t	theoretical electron-beam diameter
d_v	virtual source diameter
f	fractional factor
h	Planck's constant, 6.63×10^{-34} joule-sec
$h_i(\theta)$	angular distribution of an individual electron energy level inside the metal
l_a	photon absorption length
t	insulation layer thickness

t_g	gate metal thickness
t_{opt}	optimum film thickness
r	radius
z	axis normal to the photocathode plane
ΔE	electron energy spread
ΔI	AC signal current
ΔV	AC signal voltage
$\Delta\Phi$	work function lowering
Φ	work function
Γ	constant of a matrix element combining the initial and final states
Ω	solid angle
$\Psi(r,z)$	potential
α	coefficient of absorption
α_h	convergence half-angle of the beam
α_{PE}	part of the absorption of the electrons excited above the vacuum level having a possibility to escape
β	emission surface topography related field factor
ε_0	vacuum permitivity
ϕ	emission angle
$\eta(E, h\nu)$	energy distribution with respect to vacuum level
$\eta'(E, h\nu)$	energy distribution with respect to the Fermi level
λ	wavelength
ν	frequency
θ	solid angle of an electron momentum inside metal
θ_0	maximum solid angle of candidate electrons inside metal
κ	materials related constant

ξ	electrical field
τ	exposure time

List of acronyms

ADC	angular distribution curve
ASIC	application specified integrated circuit
CD	critical dimension
COO	cost of ownership
CTE	coefficient of thermal expansion
CVD	chemical vapor deposition
CW	continuous wavelength
DRAM	dynamic random access memory
EBL	electron-beam lithography
EDC	energy distribution curve
FED	field emission display
FIB	focused ion beam
GaAs	gallium arsenide
IC	integrated circuit
ITRS	International Technology Roadmap for Semiconductors
LIA	lock-in amplifier
LDP	laser-driven photocathode
MPU	micro-processor unit
NEA	negative electron affinity
NGL	next generation lithography
SEM	secondary electron microscopy
UV	ultraviolet

Abstract

Thin-Film Gated Photocathodes for Multiple-beam Electron-beam Lithography

Zeting Pei

Ph.D., Oregon Graduate Institute of Science and Technology
February 2001

Supervising Professor: Dr. C. Neil Berglund

When the dimensions of the silicon transistor go below 70 nm, it is generally believed that current optical lithography will not meet the resolution requirements. Electron-beam lithography (EBL) provides a potential alternative solution at these dimensions. However, present EBL systems can't provide acceptable throughput. To obtain high throughput as well as high resolution, multiple electron-beam systems will be required.

Thin-film gated photocathodes provide a promising technology for such multiple-beam, high throughput EBL systems. These devices use a thin-film photoemitting material on a transparent substrate which is illuminated by a continuous wavelength (CW) ultraviolet laser with wavelength of 257 nm from the backside of the substrate. The photoemitted electron-beams are modulated electrically by a thin-film gate constructed above the photocathodes. This novel structure removes the complex optical system that is necessary for other photocathode approaches. The simplicity of defining and scaling the electron-beam size, the potential high brightness, and the compatibility with conventional silicon

processing make gated photocathode arrays an attractive approach for multiple-beam electron-beam lithography.

This thesis carried out a detailed study of thin-film gated photocathodes. Energy distribution curves (EDC) and angular distribution curves (ADC) of photoemission from gold thin films were first studied theoretically and experimentally to understand and model the emission characteristics from thin-film photoemitters. A theoretical model for gated photocathodes based on these EDC and ADC results was developed to address the operational principles and to calculate currents as a function of gate voltage for a variety of conditions. Different device fabrication schemes were examined, and once a successful scheme was demonstrated ten different gated photocathodes with different geometry configurations were fabricated for detailed experimental characterization. The excellent agreement between theoretical and experimental results verifies the theoretical model that was developed for gated photocathodes. Extrapolation of the experimental results suggests that arrays of such devices can efficiently modulate emitted currents without interference between them with the application of only a few volts to the gates. From this study, it can be concluded that arrays of thin-film gated photocathodes offer an attractive option for use in multiple-beam electron-beam lithography.

Chapter 1
Introduction

When the dimensions of the silicon transistor go below 70 nm and beyond, the current optical lithography methods will not meet the resolution requirements. A next generation lithography (NGL) tool will be required. This dissertation presents an investigation of one such NGL candidate: thin-film gated photocathodes for multiple-beam electron-beam lithography. The use of thin-film photocathodes has been proposed as part of a NGL tool, in which arrays of independently modulated electron-beam sources are achieved by varying the incident light energy reaching each photocathode. For many applications, however, the optical complexity of such a scheme limits the attractiveness of the photocathode approach. Here a novel gated photocathode structure (Fig. 1) is presented as a solution. A thin film (10-15 nm) of gold is used as the photocathode and is backside illuminated by a continuous wavelength (CW) 257 nm ultraviolet (UV) laser. The photoemitted electron-beam is modulated electrically by a thin-film gate constructed above the photocathode.

Thin-film gated photocathodes posses several advantages over the traditional electron sources: (1) Multiple electron-beams can be created by patterning the photocathodes, with the size of each beamlet determined during the fabrication process; (2) Each electron-beam can be modulated independently, and extinguished completely by applying a negative voltage to the gate relative to that on the cathode; (3) High beam current is potentially achievable through a combination of high quantum efficiency photoemission materials, high power illumination, and a thin insulating layer between

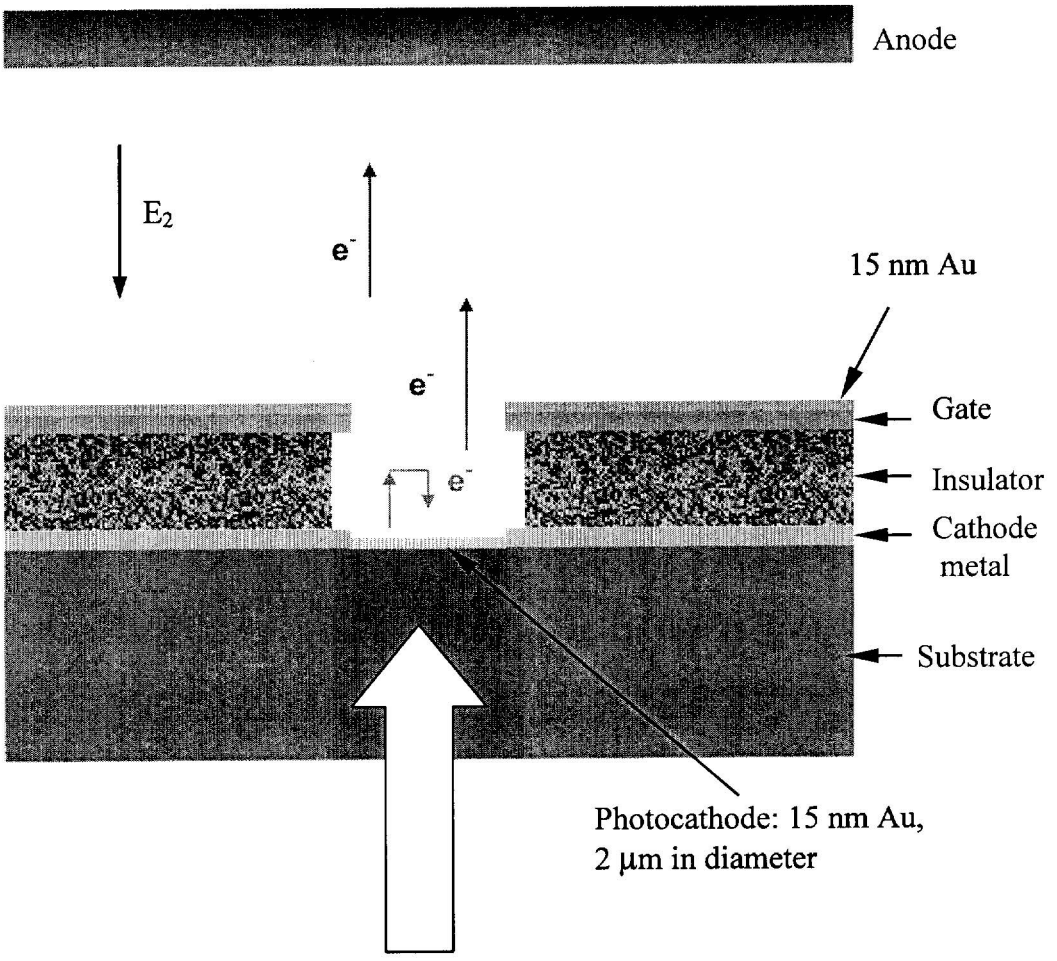

Figure 1.1 Cross-sectional diagram of a thin-film gated photocathode

the gate and the cathode; (4) Thin-film gated photocathodes can be fabricated by conventional silicon device fabrication processes.

The objective of this dissertation is to characterize and analyze the thin-film gated photocathode. Specifically, the following chapters (1) Demonstrate the concept and feasibility of thin-film gated photocathodes; (2) Present the photoemission properties of a thin-film of gold; (3) Summarize experimental characterization of the detailed current-voltage dependencies; and (4) Present a theoretical model to explain the experimental results.

Chapter 2 provides background information on the limitations of optical lithography and the fundamentals of electron-beam lithography. Also, a comparison is made of different proposed high throughput lithography systems.

In Chapter 3, the photoemission properties of thin films of gold are presented. A bulk model, the three-step model, is reviewed from the perspective of photocathode materials. The bulk model is then used to derive theoretical energy distribution curves (EDC) and angular distribution curves (ADC). Finally, the EDC's and ADC's of thin-film gold are measured.

Chapter 4 is a theoretical study of the thin-film gated photocathode. A closed form analytical solution of the electric field for the scheme of thin-film gated photocathodes was used. A typical ray tracing method was used to calculate the emission angle as a function of electron energy for a given field. The current as a function of gate voltage were then calculated by integrating the EDC and ADC functions. This model predicted a flat I-V relationship for high gate voltages. However, in general, the experimental results showed a finite slope for high gate voltages. Agreement was obtained after Schottky effect was considered. The final model is useful in predicting the behavior of gated photocathodes.

An experimental study of the thin-film gated photocathode is presented in Chapter 5. Thin-film gated photocathodes with different geometric configurations were fabricated by a combination of vacuum thermal evaporation and a focused ion beam

(FIB, FEI 610) workstation (for milling the holes). The current-voltage characteristics were measured with a lock-in amplifier (LIA).

In Chapter 6, an addressable array of thin-film gated photocathodes is proposed. The operational principles and the fabrication issues of an array are outlined. As an extension to this thesis, the addressable array of thin-film gated photocathodes should bear more practical value.

Chapter 7 summarizes the most important results. Based on this systematic study, it can be concluded that thin-film gated photocathodes are feasible and are ideal cathodes for multiple-beam, maskless, direct writing, electron-beam lithography systems.

In summary, because the concept and the structure of the thin-film gated photocathodes are novel and there is no previous work in this area, this dissertation provides original and unique knowledge to the field of electron-beam lithography. The results and conclusions of this dissertation are applicable to the practical applications.

Chapter 2

Electron-Beam Lithography Systems: Background and Status

The minimum dimension of semiconductor devices is steadily scaling down, which challenges the fabrication methods continuously, especially lithography technology. When the critical dimension (CD) of the silicon transistor goes to 70 nm and beyond, the optical lithography will not meet the resolution requirements. A NGL tool is needed [1]. Electron-beam lithography (EBL) provides an alternative solution for high resolution manufacturing of integrated circuits (IC). The wavelength of an electron-beam can be made infinitely small, and can thus theoretically provide the highest resolution.

To date, several EBL systems with a nanometer scale resolution have been developed [2]. Unfortunately, the throughput of present EBL systems is too slow to meet the requirements of cost-effective IC manufacturing. A typical production rate for a 300-mm-diameter wafers is 60 wafers/hr or 11.8 cm^2/sec, including writing and overhead, which is at least an order of magnitude faster than any combination of electron-beam tool and process demonstrated to date. Throughput of present EBL is mainly limited by the total beam current and pixel delivery rate. The fact that, on a wafer, the number of pixels and shapes has been increasing exponentially at a rate of 2x every three years makes the conventional electron-beam technology fall farther and farther behind. The present EBL systems are used principally in making masks to support optical lithography [3].

The general strategy to improve the throughput of EBL is to create multiple-beam, maskless, direct writing electron-beam systems. Several approaches have been proposed for multiple-beam electron-beam systems. The advantage and disadvantages of these systems will be compared in the next sections. This chapter is completed by the introduction of a novel approach to multiple electron-beam lithography systems: the thin-film gated photocathode.

2.1 Optical lithography and its limitations

Optical lithography has long been successfully used to pattern micro-electronic devices onto a semiconductor chip. The method has proved to be cost effective and capable of sub-micron resolution. In optical lithography, a light sensitive photoresist is spun onto a semiconductor wafer forming a thin layer on the surface. The photoresist is then selectively exposed by shining UV light through a mask. The mask contains the pattern information for the particular layer being fabricated. The resist is then chemically developed and pattern transfer from the mask to the wafer is complete.

The primary objective of lithography is to create the patterns of the desired sizes and shapes, or in other words, to define the devices on a silicon wafer. Optics is one of the key ingredients of image formation. The resolution of optics determines the minimum feature size that can be imaged. Resolution is proportional to photon wavelength. To obtain the smallest linewidths or the highest resolution, the shortest optical wavelength should be used. The present 193 nm excimer laser lithography or phase shifted 248 nm system is expected to be able to process wafers with 100 nm micro-processor unit (MPU) gate lengths [4].

There are limits to the resolution. First, at wavelengths between 20 nm and 193 nm, all materials are highly absorbing. This limitation has twofold effects: (1) There is no effective optical lens capable of transmitting or focusing light of such small wavelengths; (2) The photoresist has to be thin compared with the present thick

photoresist (having a 4:1 aspect ratio, thickness to feature size). A thinner photoresist will have reduced ability to mask the semiconductor. There are no obvious solutions to these problems [1].

2.2 Electron-beam lithography (EBL) fundamentals

Traditional EBL systems were developed from the scanning electron microscope (SEM). The EBL systems usually can provide much higher resolution than other technologies. Almost from the very beginning, sub-100 nm resolutions were reported: A 50 nm line was patterned by using a 10 nm width electron-beam in 1964 [5]. Later in 1976, with improved electron optics, 8 nm lines in Au-Pt were reported using a 0.5-nm probe and a 10 nm thick carbon membrane substrate [6]. The resolution of electron-beam lithography has yet to be surpassed by other forms of lithography technology.

2.2.1 Electron sources

The performance of a EBL system is largely related to the properties of the electron source which can be measured by three parameters: (1) Brightness, B, the current density per unit solid angle; (2) Virtual size diameter, d_v, the smallest imaginary source size from which the electron rays come; and (3) Energy spread, ΔE, the difference of the maximum energy and the minimum energy of the emitted electrons.

The current density in the electron beam at crossover represents the current that could be concentrated into a focused spot on the wafer if no aberrations were present in the electron lenses. The brightness at crossover is usually used as the source brightness [7,8],

$$B = J / \Omega \qquad (2.1)$$

$$J = \frac{I_b}{\pi(d_0/2)^2} \qquad (2.2)$$

$$\Omega = 2\pi(1-\cos\alpha_h) \qquad (2.3)$$

where J is the current density at crossover, I_b is the beam current, d_0 is the beam size at crossover, Ω is the solid angle of spread of the beam, measured by the area on the surface of a sphere of unit radius with half-angle of α_h, convergence angle (divergence angle). Ω is proportional to ΔE and inversely proportional to the accelerating voltage. Practically, for a high accelerating voltage (>10 kV), α_h is very small (~mrad), Equation (2.2) is reduced to,

$$\Omega = \pi\alpha_h^2 \qquad (2.4)$$

Thus the brightness in can be expressed by inserting Equation (2.2) and (2.4) into (2.1),

$$B = \frac{4I_b}{\pi^2 d_0^2 \alpha_h^2} \qquad (2.5)$$

The brightness required for electron beam lithography is $2\text{x}10^6$ A/(cm^2 sr). High beam current, small beam size (or small virtual source size, proportional to the beam size), small energy spread, and high accelerating voltage generally result in a high brightness, and therefore a high throughput system. A smaller virtual size and energy spread will result in higher resolution (will be explained in detail in next section).

The ability to resist contamination and ensure a long-term stability, on the other hand, is critical to the electron source for EBL systems. All of the electron sources are sensitive to the surface contamination, which causes the work function change.

However, only a moderate vacuum can be kept in EBL due to various chemical reactions [2].

Historically, three sources have been used for electron-beam systems; thermionic, field emission and thermal field emission. A thermionic source operates at a very high temperature, e.g. 2700 K for tungsten sources, whereby electrons are thermally activated and overcome the surface potential barrier to be emitted. The emitted electron current density is given by [9]

$$J = A^{**}T^2 e^{-\Phi/kT} \qquad (2.6)$$

where $A^{**} = 1.2 \times 10^6$ amp/meter^2 kelvin^2, is Richardson's constant for the materials, T is the temperature, and Φ is the potential barrier, work function, defined as the energy difference between the Fermi energy and the vacuum level. The work function is usually assumed to be a constant but several effects should be considered: (1) A temperature dependency due to thermal expansion; (2) The crystallographic plane; (3) The modification of the emission probability by surface contamination.

Higher temperatures can deliver greater beam current due to the exponential dependency of 1/T, but high temperature sacrifices the lifetime of the source. The Lanthanum hexaboride (LaB_6) source is one of the most popular cathode materials for a thermionic source. Owing to its low work function and low sublimation rate, LaB_6 can deliver a high stable brightness beam at a lower temperature (around 1800 K) for 1000's hours.

Field emission employs an extremely strong electric field ($> 3 \times 10^9$ V/m), and the surface potential barrier becomes so thin (~10 Å) that quantum-mechanical tunneling can occur through it. The electrons of the Fermi energy thus have a finite transmission probability. The field emission current density is given by Fowler-Nordheim formula [9],

$$J = \kappa \xi^2 \exp(-\beta\Phi/\xi) \qquad (2.7)$$

where κ is materials related constant and β is an emission surface topography related field factor, both need to be defined experimentally, and ξ is the electric field. Field emission is also known as cold emission (opposite to thermal emission). Field emission sources have to be operated in an ultra-high vacuum, 10^{-10} Torr or better, and they are not stable in a low vacuum due to the adsorption of environmental atoms and molecules.

From the mechanisms of thermionic emission and field emission, electron emission probability can be improved by a combination of heat and field. Such an electron source has been used in practice, known as the thermal field emission source [10]. The high current density can be obtained at a lower temperature than the thermionic source.

The laser driven photocathode, as an alternative electron source, is causing expanding interests, mainly because of its easiness to generate multiple electron-beams from a thin-film photocathode. Owing to the development of high-power and short wavelength laser technology, it is possible to develop high brightness and high current sources from laser-driven photocathodes. Below the space charge limit on photocurrent flux is given by the well-known relation,

$$J = QE\frac{e\lambda}{hc}\frac{P_i}{\pi r^2} \qquad (2.8)$$

where QE is quantum efficiency, the ratio of electrons emitted to photons illuminating the cathode), P_i is the incident optical power at wavelength λ, and e, h, and c have the usual meanings of electron charge, Plank's constant and velocity of light, r is the radius of the illumination spot size. If an EBL system uses a gold thin-film photocathode, a 257 nm UV laser illumination, and an accelerating voltage of 50 kV, the quantum efficiency is $1x10^{-4}$, the convergence half-angle is 10 mrad, and the source emission angle is 3.5 mrad [11]. To obtain a brightness of $3x10^6$ A/(cm^2 sr) on the substrate (wafer) or a photocathode brightness of $1x10^7$ A/(cm^2 sr), an incident optical power of 2.7 mW is needed to drive an illumination spot size of 300 nm in diameter.

Because of application requirements, mainly long-term stability due to work function changes caused by contamination, there are not many choices of electron sources for EBL systems. The thermionic source is the major cathode for EBL systems. Field emission sources are seldom used for EBL systems. Table 2.1 summarizes the major properties of these electron sources.

Table 2.1 Major properties of the electron sources [2,11]

Source type	brightness ($A/cm^2/Sr$)	source size	energy spread (eV)	vacuum requirements (Torr)
tungsten themionic	$\sim 10^5$	~25 μm	2-3	$\sim 10^{-6}$
LaB_6	$\sim 10^6$	~10 μm	2-3	$\sim 10^{-8}$
thermal field emission	$\sim 10^8$	~20 μm	0.9	$\sim 10^{-9}$
tungsten field emission	$\sim 10^9$	~5 nm	0.22	$\sim 10^{-10}$
photocathode	required: $2\text{-}4 \times 10^6$ exp. status: 0.2×10^6	required: 300 nm exp. status: 1.3 μm	0.5	$\sim 10^{-8}$

2.2.2 Resolution of EBL systems

The resolution of an EBL system can be defined by the final electron-beam size [12]. The theoretical beam size of an EBL system can be determined by several contributions, including the virtual source size, spherical aberrations, chromatic aberrations and diffraction effects. If any one of the factors exists in the system, the beam size can be defined solely by that contributor as follows.

Virtual size: the beam diameter is the ratio of the virtual source size, d_v, to the column demagnification, M (M<1):

$$d_g = Md_v \qquad (2.9)$$

Spherical aberrations: caused by the imperfectness of the lens and result in the tendency of the outer zones of the lenses to focus more strongly than the center of the lens:

$$d_s = 1/2C_s\alpha_h^3 \qquad (2.10)$$

where C_s is the spherical aberration coefficient of the final lens and α_h is the convergence half-angle of the beam at the target.

Chromatic aberrations: caused by the energy spread of the electrons. The lower energy electrons being focused more strongly than higher energy electrons. For a chromatically limited beam, the diameter is:

$$d_c = C_c\alpha_h\Delta E/V_b \qquad (2.11)$$

where C_c is the chromatic aberration coefficient, ΔE is the energy spread of the electrons, and V_b is the beam voltage.

Diffraction effects: quantum mechanics gives the electron a wavelength $\lambda = 1.2/(V_b)^{1/2}$ nm. This wavelength can limit the beam diameter by classical diffraction effects in very high resolution systems. For a diffraction limited beam, the diameter is given by:

$$d_d = 0.6\lambda / \alpha_h \qquad (2.12)$$

Consideration of these contributions, results in a theoretical beam size of a system:

$$d_t = (d_g^2 + d_s^2 + d_c^2 + d_d^2)^{1/2} \qquad (2.13)$$

However, these limiting factors are prominent for different sources. In general, both the virtual source size and the demagnification dominate beam diameters. In addition, systems with thermionic sources have beam diameters limited by spherical aberrations. Chromatic aberration dominates in field emission systems.

2.2.3 Throughput of EBL systems

There are several factors affecting throughput of an EBL system: total beam current, pixel delivery rate, stage velocity and resist sensitivity. The combination of beam current and resist sensitivity fundamentally determines the throughput of EBL [13]. One way to estimate the throughput is to calculate the exposure time, τ, [14]

$$\tau = QA / I_b \qquad (2.14)$$

where A is the area on the wafer to be exposed, Q is the charge dose needed for the exposed regions, I_b is the beam current. A shorter exposure time results in a higher throughput. It is clear that throughput can be improved by using sensitive resist (needing a smaller charge dose) and by using a high beam current. For a given resist, throughput can only be improved by increasing the total current delivered.

The increasing beam current is ultimately limited by stochastic Coulomb interaction between individual particles in the beam [15]. With increasing current density, the Coulomb interaction manifests itself in three effects: the space charge effect, the trajectory displacement effect, and the energy spread effect. The space charge effect stands for the deflection by the total, averaged charge of all other particles in the beam. For a uniform charge distribution in a round beam, the deflection is proportional with the distance to the axis, causing a defocus of the beam. For non-uniform distributions, the effect can cause aberrations. The space charge effect increases linearly with the beam current. The trajectory displacement effect represents the lateral shift in particle positions and the change in the velocity component perpendicular to the beam axis. It causes a direct deterioration of the system resolution. Energy broadening is the change in axial velocity resulting from the same individual interactions and affects the system resolution via the chromatic aberration of lenses and deflectors.

Due to these effects, the maximum currents in today's fastest tools are limited to ~1 μA. As the required device dimensions on integrated circuits are reduced, the average current available from a shaped beam tool will correspondingly decrease. It is very difficult to improve throughput by increasing beam current using conventional EBL [13].

2.3 Conventional EBL Systems: architecture and writing strategies

Electron beam lithography systems have been developed for two applications: mask making and direct write of chips on silicon [16]. A mask is made by coating a

chrome clad glass plate with an electron-beam sensitive resist layer which is subsequently exposed and developed to generate the required pattern on the mask. The direct writing systems are for advanced prototyping of integrated circuits and manufacture of small volume specialty products, such as gallium arsenide (GaAs) integrated circuits and optical wave-guides.

The architecture of the convention single beam EBL systems can be divided into three categories: Gaussian beam (or round beam), shaped beam and cell projection [17,18]. Most early EBL systems [19] employed a Gaussian beam, that is, a beam whose intensity varies approximately as a Gaussian profile with radius from the center of the beam. The resolution of Gaussian beam systems can be very high from a few nm to 100 nm. Vector scanning mode is preferred in Gaussian beam systems where the Gaussian ray scans only the exposed areas. The throughput of Gaussian beam systems is very low.

A second and much more popular electron-beam lithography method is to produce a variable shaped beam. The shaped beam has a uniform current density distribution which can be made from a conventional electron source by using a square aperture [20, 21]. The resolution of the shaped beam is determined only by the edge slope of the intensity distribution, whereas the resolution of Gaussian beam is also determined by the variation due to the demagnified Gaussian source. The shaped beam systems can obtain the same resolution as the Gaussian beam but reduces the redundant data need for Gaussian beam systems. Therefore the throughput of shaped beam system is higher than that of Gaussian beam systems with the same electron source.

Another architecture used to improve the throughput is the cell projection system. The cell projection system uses a patterned aperture. The pattern is printed on the wafer directly. As a result, the electron-beam shot number is reduced and throughput can be improved [22]. This kind of system, however, is useful only for the simple structure IC, such as dynamic random access memory (DRAM).

2.4 High throughput electron-beam lithography systems

2.4.1 General considerations

Multiple-beam electron-beam, maskless, direct writing technology is the standard approach to high throughput EBL systems. The array of electron beams provides several benefits: (1) The data rate is significantly improved; (2) The current required for each beam is minimized; (3) An individual beam can be made scalable with the device dimensions; (4) In some approaches [23], the total current can be increased without inducing Coulomb interaction by using a large number of miniature cathodes. High throughput as well as high resolution can be obtained by using multiple electron-beam systems.

Several approaches of multiple electron-beam lithography have been proposed for high throughput EBL systems [11, 23-30], but no system has been built so far. Although there does not appear to be any physical limitation to build such a system, several issues may need to be considered for practical systems. First, the complexity of the system has to be well managed. Proposed multiple beam systems aim for hundreds or thousands of electron-beams. To control the individual beam as well as all of the beams very well is very challenging. The beam uniformity is critical to this issue. Second, the system has to have a reasonable cost of ownership (COO). High throughput is also a basic requirement. The electron source should have reasonable lifetime and should function stably in a contaminated environment. Maintenance should not impact the production.

2.4.2 Promising approaches

There are two generic approaches to multiple electron-beams: multicolumn and multisource [13]. In the microcolumn approach [23], multiple electron-beams are

created through the use of an array of closely spaced, miniature electron-optic columns. Each column contains a single Schottky emission cathode. The microcolumns typically operate at 1 keV and deliver either a Gaussian or shaped beam. Patterns can be written with the beam scanned over only a narrow trip ($\leq$0.1 μm) with a laser-controlled stage moving continuously in the orthogonal direction to build up the complete chip pattern. This approach allows individual calibration of each beam for potentially higher accuracy; there are no space charge limits to the number of beams or total current, and no beam-to-beam uniformity issues due to lens aberrations. Considerable progress has been made in advancing the base technologies for the microcolumns [29]. However, controlling a large number of such microcolumns, say one thousand, becomes an enormous practical issue. Further, the overall system reliability and the maintenance of a system with large numbers of microcolumns may impose a big problem.

In the typical multisource approach [11,26-28], the electron sources use an array of independently modulated electron-beams formed by laser-driven photocathodes (LDP) to achieve multiple beams. The emitted electrons are collected, collimated, and demagnified in a conventional electron-optical column configuration to form an array of beamlets. This array is scanned across the substrate in a high-speed raster mode by magnetic and/or electrostatic deflection fields to expose resist-coated wafers [11]. A large number of electron-beams can be produced from the flat, uniform surface of photocathodes by using multiple laser-beam patterning technology. The electron-beams have similar properties and good consistency in the array. The beam current can potentially be high by using a high power illumination and a high quantum efficiency photocathode. The Coulomb interaction can be minimized by optimizing the column design, the number of beamlets, and the beamlet array size to achieve high throughput as well as desired resolution [11]. These factors together with a high modulation frequency result in a high data delivery rate and therefore improve the throughput.

The success of using thin-film photocathodes as the electron source also depend on the optical system, which defines the electron-beam size and modulates the electron

beam at a high frequency. However, one drawback of this approach is the optical system for a large number of electron-beams, which is very complex.

Besides the photocathode [26-28], an addressable field emission array was also reported as a multisource [31]. The device consists of a two dimensional array of miniature planar field emission cathodes consisting of a low electron affinity coating deposited on aluminum biasing pads controlled by CMOS circuitry. Each cathode is individually addressable, providing a matrix of massively parallel but independent electron beams. The detailed operation condition and I-V characteristics were not reported. The success of this approach will depend on two issues: the stability of this type of field emitter in a contaminated environment and the magnitude of the beam current.

Another more rigorous approach is the so called Multi-column Multi-beam (MxM) system, which combines multicolumn and multisource approaches in one system [32]. The system consists of multiple columns with multiple beams per column. The electron optics combine microfabrication of the cold field emitter source, apertures and blankers with a compact electrostatic column design for the scanning and imaging. Although the system is scheduled to meet the International Technology Roadmap for Semiconductors (ITRS) 70 nm node and is expected to extend to 35 nm, several problems still remain: (1) The stability from the cold field emitter is not stable; (2) The presence of fast transition noise; (2) The complexity of the structure (this was not addressed).

As no system has been built based on these approaches, it is hard to say which is the best. Table 2.2 compares the two major approaches. It is obvious that cost effective and low COO multiple beam EBL systems may be built using a multisource approach based on the photoemission technology. Thin-film gated photocathodes technology is thus more attractive due to its simplicity and efficiency.

Table 2.2 Comparison of two approaches: multicolumn and multisource

	advantages	disadvantages
multicolumn	1. no space charge limits, high total current 2. individual calibration of each beam , potential high accuracy	1. complex to control large number of columns 2. difficult to maintain
multisource	1. large beam number, high pixel delivery rate 2. easy multiple beam generation 3. good beam uniformity; 4. low cost source; 5. reliable and easy to maintain;	1. complex optical system 2. throughput ultimately limited by Coulomb interaction

Summary

Multiple-beam electron-beam systems are generally favored for next generation EBL tools because of throughput and resolution considerations. The thin-film gated photocathode studied in this thesis was proposed as an alternative electron source for the multi-source approach. It removes the complex optical system of its counterpart, the thin-film photocathode. The concept and advantages of this approach have been described in the previous chapter and the rest of this study. The thin-film gated photocathode concept can be extended to an addressable array of gated photocathodes, as described in Chapter 6. Thin-film gated photocathodes may offer an attractive option for use in multiple-beam lithography.

References

[1] P. Burggraaf, "Optical lithography to 2000 and beyond," Solid State Technology, **42 (2)**, pp. 31-41, 1999.

[2] M. A. Mark, and M. J. Rooks, "Electron beam lithography," in Handbook of Microlithography, Micromachining, and Microfabrication, Volume 1, SPIE Optical Engineering Press, Ed. by P. Rai-Choundhury, pp. 139-251, 1997.

[3] H. J. Levinson, and W. H. Arnold, "Optical lithography," in Handbook of Microlithography, Micromachining, and Microfabrication, Volume 1, SPIE Optical Engineering Press, Ed. by P. Rai-Choundhury, pp. 11-138, 1997.

[4] P. Burggraaf, "2000 begins with a revised industry 'Roadmap'," Solid State Technology, **42 (1)**, pp. 31-44, 1999.

[5] A. N. Broers, "Micromachining by sputtering through a mask of contamination laid down by an electron beam," Proceedings of the First International Conference on Electron and Ion Beam Technology, Ed. by R. Bakish, Wiley, New York, pp. 191-204, 1964.

[6] A. N. Broers, W. W. Molzen, J. J. Cuomo, and N. D. Wittels, "Electron-beam fabrication of 80-A metal structures," Applied Physics Letter, **29**, pp. 596-598, 1976.

[7] Miklos Szilagyi, Electron and Ion Optics, Plenum Press, New York, p. 286, 1988.

[8] J. I. Goldstain, *et al.*, Scanning Electron Microscopy and X-Ray Microanalysis, Plenum Press, New York, p. 20, 1981.

[9] J. S. Blakemore, Solid State Physics, 2nd edition, Cambridge University Press, Cambridge, pp. 188-196, 1985.

[10] M. Gesley, "Thermal-field-emission electron optics for nanolithography," J. App. Phys., **65,** pp. 914-926, 1989.

[11] M. Mankos, S. Coyle, A. Fernandez, A. Sagle, P. Allen, W. Owens, J. Sullivan and T. H. P. Chang, "Multisource optimization of a column for electron lithography," J. Vac. Sci. Technol. B **18**, pp. 3010-3106, 2000.

[12] M. Sato, "Resolution," in Handbook of Charged Particle Optics, Ed. by Jon Orloff, CRC Press, Boca Raton, p. 319, 1997.

[13] M. A. McCord, "Electron beam lithography for 0.13 μm manufacturing," J. Vac. Sci. Technol. B **15**, pp. 2125-2129, 1997.

[14] G. Owen, and J. R. Sheats, "Electron beam lithography systems," in Microlithography, edited by Sheats, J. R. and Smith, B. W., Marcel Dekker, Inc., p. 367, 1998.

[15] P. Kruit, and G. H. Jansen, "Space charge and statistical coulomb effects," in Handbook of Charged Particle Optics, Ed. by Jon Orloff, CRC Press, Boca Raton, p. 275, 1997.

[16] F. J. Hohn, "Electron beam lithography, direction in direct write and mask making," in Electron-Beam, X-Ray, and Ion-Beam Technology: Submicrometer Lithographies IX, Proceedings of SPIE Vol. 1263, San Jose, CA, pp.152-163, 1990.

[17] C. N. Berglund, "Multi-electron beam lithography," presented in Intel-OGI seminar (4/6/00).

[18] T. H. Newman, R. F. W. Pease, and W. Devore, "Dot matrix electron beam lithography," J. Vac. Sci. Technol. B **1**, pp. 999-1002, 1983.

[19] P. Riemenschneider, et al, "EBS-5: A vector scan electron beam lithography system for research applications," J. Vac. Sci. Technol., B **4**, pp. 68-72, 1986; M. Hassel, et al, "Development of nanometric electron-beam lithography system (JBX-5D II)," J. Vac. Sci. Technol., B **4**, pp. 64-67, 1986.

[20] H. C. Pfeiffer, "New imaging and deflection concept for probe-forming microfabrication systems," J. Vac. Sci. Technol. **12**, pp. 1170-1173, 1975.

[21] H. C. Pfeiffer, et al., "EL-4, a new generation electron-beam lithography system," J. Vac. Sci. Technol. B **11**, pp. 2332-2341, 1993.

[22] Y. Nakayama, S. Okazaki, N. Saitou, and H. Wakabayashi, "Electron-beam cell projection lithography: A new high-thoughput electron-beam direct-writing techonology using a specially tailored Si aperture," J. Vac. Sci. Technol. B **8**, pp.1836-1840, 1990.

[23] T. H. P. Chang, et al, "Electron-beam microcolumns for lithography and related applications," J. Vac. Sci. Technol. B **14**, pp. 3774-3781, 1996.

[24] T. R. Groves and R. A. Kendall, "Distributed, multiple variable shaped electron beam column for high throughput maskless lithography," J. Vac. Sci. Technol. B **16**, pp.3168-3173, 1998.

where I_p is the intensity of light at a depth x from the surface, I_{p0} is the incident light intensity, R is the reflectivity, α is the coefficient of absorption which is a constant of the solid for a particular frequency, Γ is a constant: a matrix element combining the initial and final states, N_V is valence-band optical density of state (ODS), and N_C is the conduction-band optical density of state (ODS).

In the second step, electron transport was modeled by the electron-electron scattering process: only the electrons not suffering an inelastic collision can travel to the surface. The probability that an electron does not scatter before reaching the surface is given by:

$$P = e^{-x/L(E)\cos\theta} \qquad (3.4)$$

where L(E) is the electron-electron scattering length, θ is the solid angle of the electron momentum.

In the third step, an electron escapes into vacuum by overcoming the energy barrier, work function. With this constraint, not all of the excited electrons can escape, only those with a energy component in the normal direction that exceeds the work function. A candidate thus must be in the cone defined by:

$$\theta_0 = \cos^{-1}(\Phi / E)^{1/2} \qquad (3.5)$$

θ_0 defines the maximum solid angle over which an electron with energy, E, can escape. The fraction of electrons, at location, x, that escape without scattering is given by:

$$F(E,x) = \int_0^{\theta_0} \tfrac{1}{2}\sin\theta e^{-x/L(E)\cos\theta} d\theta \qquad (3.6)$$

The number of the photoemitted electrons with energy E is equal to the integration of the product of equations of (3.2), (3.3) and (3.6) for x=[0,∞]. The result is the energy distribution of photoemission.

This theory allows photoemission to be related to the photocathode parameters, such as the optical absorption coefficient, electron scattering mechanism, and the height of the potential barrier at the surface. It bridges the photoemission spectra with the electronic structure by considering the optical properties of the solid and electron transport properties.

The three step model has practical applications [8,9], and is the sole theory in photocathode engineering, e.g. the development of negative electron affinity (NEA) photocathodes [9-11]. One example is a simplified equation for prediction of the photoemission quantum yield [9],

$$QY = \frac{\frac{\alpha_{PE}}{\alpha} P_E}{1 + \frac{l_a}{L}} \qquad (3.7)$$

where $l_a=1/\alpha$ is the absorption length, l_a/L is the ratio of absorption length to scattering length, α_{PE} is the part of the absorption where the electrons are excited above the vacuum level having a possibility to escape, α_{PE}/α is the fraction of the electrons excited above the vacuum level, and P_E is the escape probability of electrons reaching the surface with sufficient energy. From this equation, one can easily see that a high ratio of l_a/L will result in a low yield, which is the case for metal in the ultraviolet region, where l_a/L is as high as 10^4.

3.1.2 Laser-driven photocathodes and their applications in electron-beam lithography

Owing to the development of high-power and short wavelength laser technology in the last two decades, it is possible to develop high brightness and high current sources from laser-driven photocathodes. Most laser-driven photocathodes use thin films of photoemission materials coated onto a substrate with back illumination. With this configuration, laser-driven photocathodes have several advantages over the conventional thermal or field emission sources: (1) No heating or high electric fields is required; (2) The electron beam can be modulated by adjusting the incident laser beam energy; (3) The electron source size and shape can be defined by the laser beam; (4) The electron energy spread is small (less than 1 eV); and (5) Multiple beams are expected to be generated with good uniformity due to the good uniformity in thickness.

These features make the laser-driven photocathodes a promising candidate source for electron-beam lithography systems. The application conditions in EBL, however, are very strict. One requirement is that the photocathodes have to have long-term stability in a moderate level vacuum, which is critical for consistency, and which guarantees high yield needed in IC manufacturing. A more practical requirement is that the photocathodes should be able to withstand exposure to air; thus no special vacuum transportation would be required for handling prior to vacuum insertion. [13]. The photoemission property relationship to surface chemistry thus has to be well understood.

Laser-driven photocathodes can be broadly divided into three groups: metal compound and matrix photocathodes, conventional semiconductor photocathodes, and metallic photocathodes [14]. Metal compound and matrix photocathodes, e.g. Ag-O-Cs, have long been used in radiation detectors and imaging tubes [10]. These photocathodes were designed to operate at low current density, usually below 1 $\mu A/cm^2$. High light level exposure results in fatigue of the cathodes, which is caused by surface ion bombardment, electrolytic effect and temperature rise [13]. These photocathodes are thus not suitable for the electron source for EBL systems. The Cs_3Sb photocathode is

known for its high quantum efficiency, 10-30%. One study using an argon ion laser showed that degradation of this photocathode was due to cesium de-sorption from the surface [14]. Metal compound and matrix photocathodes are generally disregarded for the EBL application.

Semiconductor photocathodes, especially GaAs, have been studied intensively and some of the studies were for EBL applications [11,15-18]. The proposed photocathodes were composed of a glass substrate with an upper layer of gallium arsenide. A monolayer of CsO was deposited on the surface of the semiconductor, lowering its work function. The resulting work function can be lower than the conduction band energy, thus this photocathode was named a negative electron affinity (NEA) photocathode. The most striking features of this kind of photocathode are its high current density, 1×10^8 A/cm^2, and low energy spread, 50 meV. However, the CsO layer is extremely sensitive to contamination, and therefore the current lifetime is too short for commercial applications.

Metallic laser photocathodes, due to their good electric and heat conductivity properties as well as higher damage threshold, exhibit distinct advantages over semiconductor or conventional electron sources in obtaining high beam currents. Metallic photocathodes usually have low quantum efficiency, 10^{-4} –10^{-3}, but a high power ultraviolet laser can be used to generate a high current density [19].

Laser photocathodes based on gold have been studied for a high-current source in applications of both accelerators and pulsed X-ray sources [20-23]. A KrF excimer laser with a density of 3 GW/cm^2 was used to generate a peak current density of 500 A/cm^2 in these studies.

The study of gold laser-driven photocathodes for EBL has been a recent topic and was mainly carried out at the Oregon Graduate Institute [12,24]. Gold was chosen for two reasons: (1) Gold is inert; the photoemission characteristics are relatively reproducible and stable even in contaminated environments, and the practical photocathodes are thus feasible in terms of the application criteria; (2) The work function of gold is close to the wavelength of the state-of-art laser, and thus the energy

spread of the photoemission is small. This study used a frequency doubled CW ultraviolet laser with a wavelength of 257 nm. The photocathodes are composed of thin-film gold deposited on either sapphire or fused silicon.

So far Jiang et al. [12], has investigated the optimum thickness, t_{opt}, for maximum quantum yield for the transmission model. The value of t_{opt} was measured as 15 nm for the photocathode using a sapphire substrate and a UV laser with a wavelength of 257 nm. A theoretical model to calculate t_{opt} was derived from the three-step model,

$$t_{opt} = \ln(\alpha L)/(\alpha - 1/L) \qquad (3.8)$$

where the optimum thickness is a function of photon absorption length, $1/\alpha$, and electron mean free path, L. Unfortunately, the values of α and L are not available for the wavelength of 257 nm, the comparison of the experimental and the theoretical values are impossible.

This results, however, did not agree with similar experiments previously carried out of which the optimum thickness for maximum quantum yield was measured about 10 nm for a gold film on a LiF substrate with a similar photon energy [25-27]. The discrepancy may arise from the thin-film microstructure difference or inaccurate thickness measurements.

The surface chemistry and performance of the gold thin films in a variety of gas environments have also been studied [24]. Long-term stability of up to 30 hours can be repeated with a high density laser (10 $mW/\mu m^2$), although the degradation mechanism has not been fully understood.

Fundamental photoemission properties of the energy distribution curve and the angular distribution curve are studied in this dissertation. This dissertation is not devoted to the study of the photoemission properties of gold. Instead, the goal is to characterize the electrical properties of thin-film gated photocathodes. An examination is made of only the properties necessary for characterizing the thin-film gated

photocathodes, the energy distribution curve (EDC) and the angular distribution curve (ADC) of photoemission.

3.2 Theoretical models of photoemission of gold thin films

3.2.1 Energy distribution curve (EDC) of photoemission from gold thin films

The mathematical model used in this dissertation of the energy distribution of photoemission from a thin film gold was derived by modifying Krolikowski's work [28], which was based upon the classical three-step model [6,7]. For a thin film of gold with a thickness, t_f, deposited onto a C-plane double polished sapphire substrate, with a CW UV laser (λ=257 nm) illumination from the backside, the energy distribution curve of photoemission can be re-defined from Section 3.1.1 by two modifications: (1) If x is the distance from the interface of the gold/sapphire, an electron emitted from x needs to transports a distance of t_f-x; (2) If the electron energy, E, is assumed to be with respect to vacuum level, the energy difference from the Fermi level is Φ + E. The absorbed light, I_p, has the same definition as Equation (3.2),

$$I_p = I_{p0}(1-R)e^{-\alpha x} \qquad (3.9)$$

The probability, P, of excitation of an electron to energy Φ + E from energy Φ + E-hv can be re-defined using Equation (3.3) by lumping N_V and N_C into a single optical density of states, N(Φ + E, hv),

$$P(\Phi + E, h\nu)dE = \Gamma N(\Phi + E, h\nu)dE \qquad (3.10)$$

Near threshold, as the case studied in this dissertation, the optical density of state can use a approximate form as [29],

$$N(\Phi + E, h\nu) = [E - (h\nu - \Phi)]^2 \qquad (3.11)$$

Inserting Equation (3.11) to (3.10),

$$P(\Phi + E, h\nu)dE = \Gamma[E - (h\nu - \Phi)]^2 dE \qquad (3.12)$$

The probability that an electron does not scatter before reaching the surface is defined by modifying Equation (3.4),

$$Q = e^{-(t_f - x)/L(\Phi + E)\cos\theta} \qquad (3.13)$$

The cone defined in Equation (3.5) can be rewritten as,

$$\theta_0 = \cos^{-1}\left(\frac{\Phi}{\Phi + E}\right)^{1/2} \qquad (3.14)$$

It is apparent that, for the investigated case, the minimum value of square root of $\Phi/(\Phi + E)$ is about 0.9. The following condition is a good approximation (this manipulation will simplify the following integration),

$$L(\Phi + E) = L(\Phi + E)Cos\theta \qquad (3.15)$$

Thus Equation (3.13) is simplified as,

$$Q = e^{-(t_f - x)/L(\Phi + E)} \qquad (3.16)$$

Equation (3.6), the fraction of electrons at location, x, that escape without scattering is modified as,

$$F(E,x) = \int_0^{\theta_0} \tfrac{1}{2}\sin\theta e^{-(t_f - x)/L(\Phi+E)} d\theta \qquad (3.17)$$

Upon integration, equation (3.17) becomes,

$$F(E,x) = \tfrac{1}{2}(1-\cos\theta_0)e^{-(t_f - x)/L(\Phi+E)} \qquad (3.18)$$

where θ_0 is defined by Equation (3.14). The energy distribution can be obtained by integrating the product of Equation (3.9), (3.12) and (3.18) for x = [0,t],

$$\eta(E,h\nu) = \frac{1}{2}\alpha\Gamma[E-(h\nu-\Phi)](1-\cos\theta_0)\int_0^{t_f} e^{-[\alpha x + (t_f - x)/L(\Phi+E)]} dx \qquad (3.19)$$

Upon integration, Equation (3.19) becomes,

$$\eta(E,h\nu) = \frac{1}{2}\Gamma[E-(h\nu-\Phi)]\frac{\alpha L(\Phi+E)}{1-\alpha L(\Phi+E)}[1-(\frac{\Phi}{\Phi+E})^{1/2}][e^{-\alpha t_f} e^{-t_f / L(\Phi+E)}] \qquad (3.20)$$

The electron mean free path, L(Φ+E), can be expressed as with l_e=7 nm [30,31],

$$L(\Phi+E) = l_e\Phi/(\Phi+E) \qquad (3.21)$$

The gold film work function is 4.3 eV [19]. Γ is a constant and use an arbitrary number (such as 1000 in this study). α is an unknown, however, $1/\alpha$ can be estimated as 50 nm from Equation (3.8) if L is 6-7 nm. A 257 nm wavelength photon has an energy of 4.89 eV. The EDC was calculated as Figure 3.1.

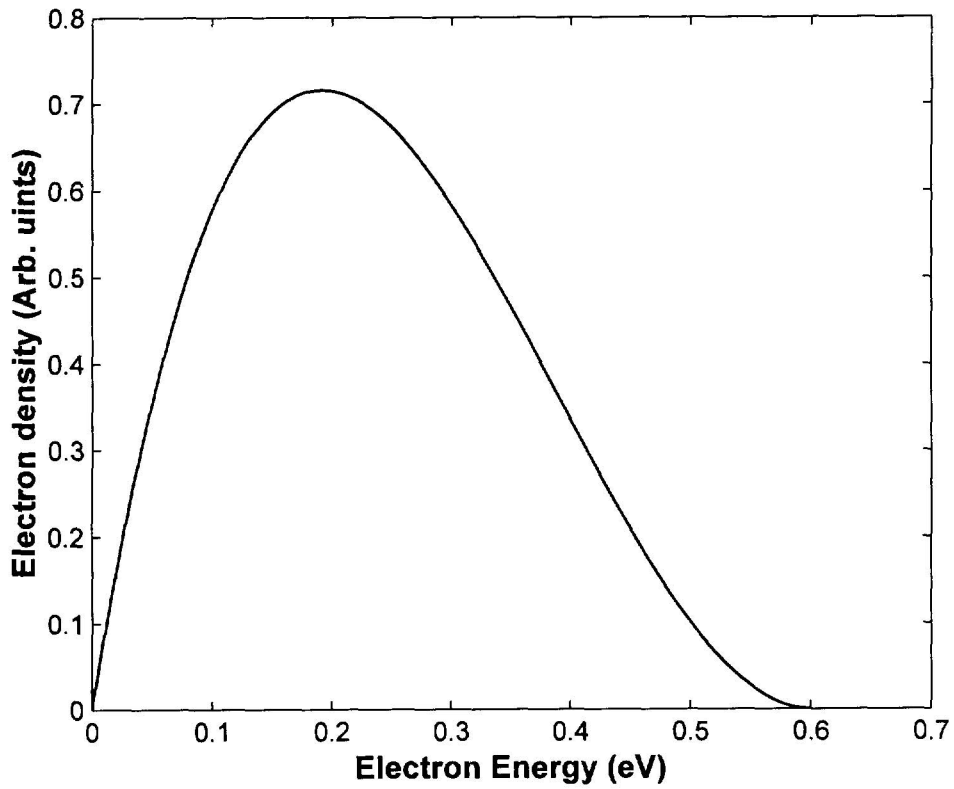

Figure 3.1 Calculated energy distribution curve of photoemission from a thin film of gold, assuming the total energy spread is 0.6 eV.

3.2.2 Angular distribution curve (ADC) of photoemission from gold thin films

The other important photoemission property is ADC. Together with EDC, the theoretical ADC will be used to calculate current-voltage characteristics of thin-film gated photocathodes. To derive the angular distribution of photoemission from a thin film of gold, the following assumptions were made: (a) Excited electrons of energy E_i are evenly distributed inside the metal; (b) Overcoming the work function, Φ, is the only contributing factor in the energy loss during the emission, and thus the candidate electrons lie in the same cone, θ_0, defined in Equation (3.5); (c) The distribution of photo-excited electrons inside the metal is independent of the thickness of the film.

Let the EDC inside the metal be defined as, $\eta'(E,h\nu)$, with respect to the Fermi level. Outside the metal, EDC is defined as, $\eta(E,h\nu)$, with respect to vacuum level. θ is the solid angle inside the metal, whereas ϕ is that of outside the metal. The two EDCs are actually identical but reference a different energy.

$$\int_0^{E_{max}} \eta(E,h\nu)dE = \int_{\Phi}^{h\nu} \eta'(E,h\nu)dE \qquad (3.22)$$

Starting from the assumptions of (a) and (b), the angular distribution of candidate electrons with energy, Ei, is,

$$h_i(\theta) = \frac{\eta'(E,h\nu)_i}{\int_0^{\theta_0} 2\pi \sin\theta d\theta} \qquad (3.23)$$

And $$\frac{d\eta'}{d\theta} = 2\pi \sin\theta . h_i(\theta) \qquad (3.24)$$

If $H_i(\phi)$ is the angular distribution of emitted electrons with energy E_i, then

$$\eta_i(E_i, h\nu) = \int_0^{\pi/2} 2\pi H_i(\phi) \sin\phi d\phi \qquad (3.25)$$

and $$H_i(\phi) = \frac{1}{2\pi \sin\phi} \frac{d\eta(E_i, h\nu)}{d\phi} \qquad (3.26)$$

Equation (3.26) can be rewritten as

$$H_i(\phi) = \frac{1}{2\pi \sin\phi} \frac{d\eta(E_i, h\nu)}{d\theta} \frac{d\theta}{d\phi} \qquad (3.27)$$

It is obvious that

$$\frac{d\eta}{d\theta} = \frac{d\eta'}{d\theta} \qquad (3.28)$$

Substituting (3.22) and (3.28) into (3.27)

$$H_i(\phi) = \frac{\eta'}{\int_0^{\theta_0} 2\pi \sin\theta d\theta} \frac{\sin\theta}{\sin\phi} \frac{d\theta}{d\phi} \qquad (3.29)$$

θ and ϕ can be correlated to each other from assumption of (b), which states that the change in the momentum component in the normal direction is attributed to the work function, Φ. The component parallel to the surface of the metal does not change.

$$\cos^2\theta = \cos^2\phi + \sin^2\phi\frac{\Phi}{E_i} \qquad (3.30)$$

Inserting (3.30) into (3.29):

$$H_i(\phi) = \frac{\eta(E_i, h\nu)}{\int_0^{\theta_0} 2\pi\sin\theta d\theta}\frac{1-\frac{\Phi}{E_i}}{\sqrt{1+\tan^2\phi\frac{\Phi}{E_i}}} \qquad (3.31)$$

Equation (3.31) is the angular distribution of emitted electrons with an energy of E_i (with respect to the Fermi level). A full picture of the angular distribution is found by integrating (3.31) over the full energy range with respect to the vacuum level.

$$H(\phi) = \int_0^{E_{max}} \frac{\eta(E, h\nu)}{\int_0^{\theta_0} 2\pi\sin\theta d\theta}\frac{1-\frac{\Phi}{\Phi+E}}{\sqrt{1+\tan^2\phi\frac{\Phi}{\Phi+E}}} dE \qquad (3.32)$$

Eq. (3.32) was computed numerically and plotted as shown in Figure 3.2. This result consists with that measured from bulk materials [39].

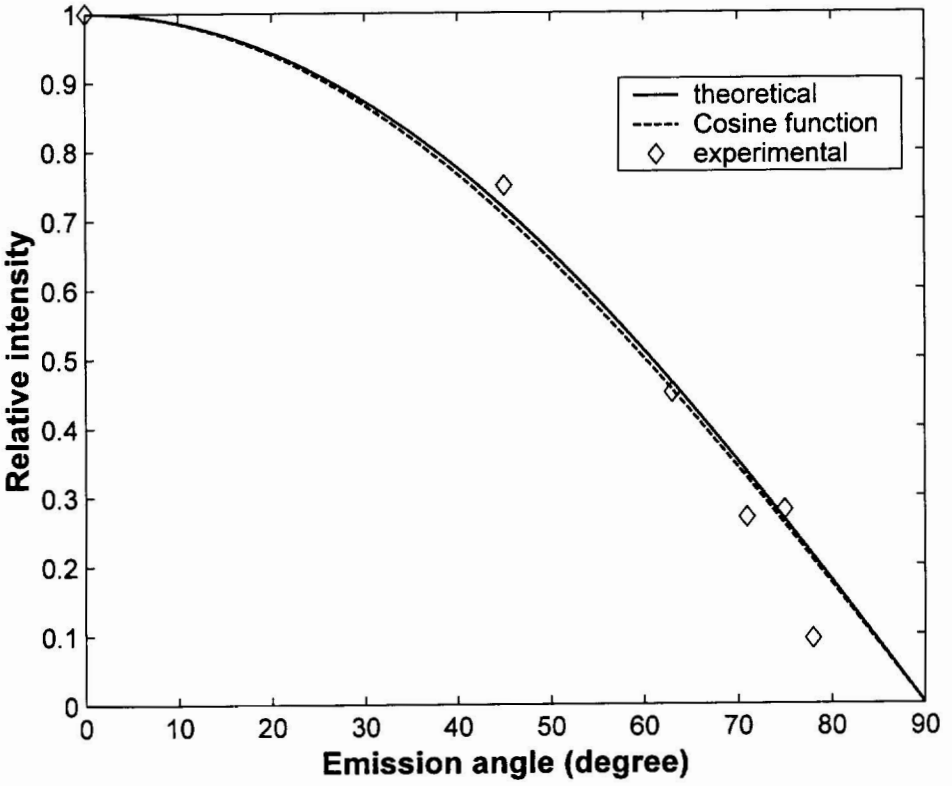

Figure 3.2 Angular distribution curve of photoemission from a thin film of gold; theoretical curve (solid line) compared with cosine function (broken line) and the experimental results.

3.3 Experimental study of photoemission of gold thin films

3.3.1 Energy distribution curve (EDC) of photoemission from gold thin films

The energy distribution curve of photoemission from a thin film of gold was measured by an AC method using retarding potentials [4,32-35]. This method is simple but reliable. In this experiment, a thin-film photocathode was illuminated from the backside. Photoemitted electrons were collected by a plain plate anode 1mm away from the photocathode. As the laser beam spot size was only 300 μm, the photoemission was thus assumed to be fully collected by the anode. To prevent any photoemission from the anode, the copper anode was coated with a 0.2 μm thick Ni-layer. If a retarding voltage, V_R, is applied on the anode, only the electrons with energy greater than $-eV_R$ can reach the anode. The measured photo-current is a function of energy distribution and anode voltage,

$$I = \int_{-eV_R}^{E_{max}} \eta(E, h\nu) dE \qquad (3.33)$$

If an AC signal with a small voltage, ΔV, is superimposed on V_R, an AC current can be measured, ΔI, proportional to the slope of I-V curve. The proportionality is defined by equation (3.33) and at the point V_R and at a frequency that is the same as that of ΔV. If ΔV is small and kept constant, the measured ΔI versus retarding voltage V_R is a true differential curve, i.e. the energy distribution curve (EDC).

The AC signal was generated by a built-in signal generator in a lock-in amplifier (LIA). The LIA can measure the resulting ΔI from a resistor by its phase detection feature. The AC signal can be superimposed onto the retarding potential by an inductor [4] or simply using an Op-amp: where a unit gain is set and the AC is connected to one

input, the retarding voltage to the other, and the output to the anode. Identical results have been obtained from two set-ups.

The magnitude of the AC signal used in this experiment was 5 mV, the retarding voltage sweep from –1V to +1 V with a step of 100 mV. The resistor for the ΔI measurement was 1 kΩ. The measured EDC is shown in Figure 3.4. The value of half of the energy spread is less than 0.6 eV, closely matching expectations based on the independently measured work function of gold film of 4.2 eV and the 4.8 eV photon energy of illumination. A broad tail in the low energy region is believed to be due to inadvertent photoemission from the anode.

Two factors may affect the result of the measurement. One is the shape of the anode/collector. The planar anode resolves only the component of kinetic energy parallel to the field and results in a distorted EDC. For this study, however, because the photon energy is close to the gold work function, also known as the threshold photoemission, the distortion is within the range of measurement error and thus is not significant. Also, the experimental value of the total energy spread is the objective of this study. The distortion is thus not important. Another factor that can affect EDC is the voltage drop on the resistor and the capacitive current between the cathode and anode. Results of the measurements by the original circuit and an improved circuit [4] were identical, which showed that the voltage drop on the resistor and the capacitive current are insignificant, and thus the measurement is valid.

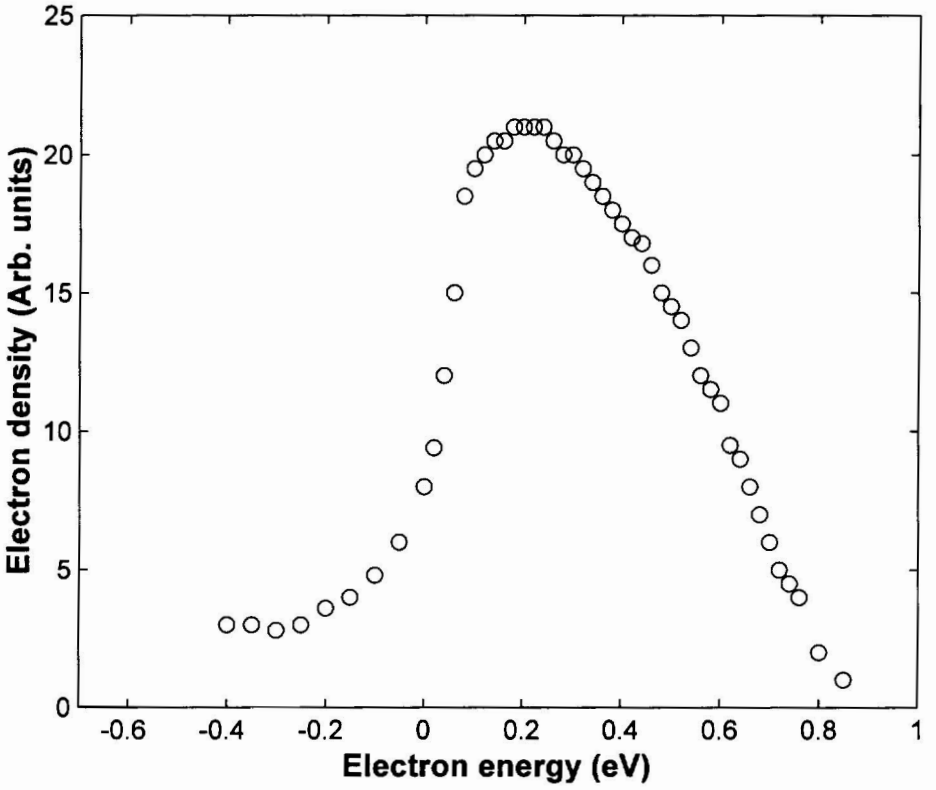

Figure 3.3 Measured energy distribution curve of photoemission from a thin film gold with an illumination of a 257 nm UV laser.

3.3.2 Angular distribution curve (ADC) of photoemission from gold thin films

The angular distribution curve (ADC) of photoemission was typically measured by an electron energy analyzer [36-38]. A simple set-up as shown in Figure 3.6 was used in this study and it is similar to experimental approaches reported by Moss [39].

The anode is a copper disc with a diameter of 30 mm. Six probes (Fig. 3.6 shows only 4) of 0.6mm in diameter were inserted into the copper disc, separated by 2 mm. These probes were coated with an in-vacuum dielectric layer, and the dielectric was trimmed off at the collection end to prevent any possible charge accumulation. The distance between the anode and cathode was 2 mm. The position of the laser beam can be precisely positioned using a high precision micrometer driven stage (2.5 μm in vertical and 5 μm in horizontal).

If the photoemission distribution J(r) in the normal direction is J_0, and in ϕ_1 is J_1, the area of probe cross section is A, the measured currents from probe 0 and 1 are I_0 and I_1,

$$I_0 = J_0 A \qquad (3.34)$$

$$I_1 = J_1 A / [\pi(r'^2 - r^2)] \qquad (3.35)$$

where r' and r are shown in Figure 3.6. Thus

$$J_0 = I_0 / A \qquad (3.36)$$

$$J_1 = I_1 [\pi(r'^2 - r^2)] / A \qquad (3.37)$$

The normalized intensity is thus:

$$J_0^{'} = 1 \qquad (3.38)$$

$$J_1^{'} = J_1 / J_0 \qquad (3.39)$$

A similar operation can be performed on probe 2 and 3. Changing the cathode-anode separation enables J(r) to be measured in multiple angles. The measured values are plotted in Figure 3.2, and compared with the theoretical curve.

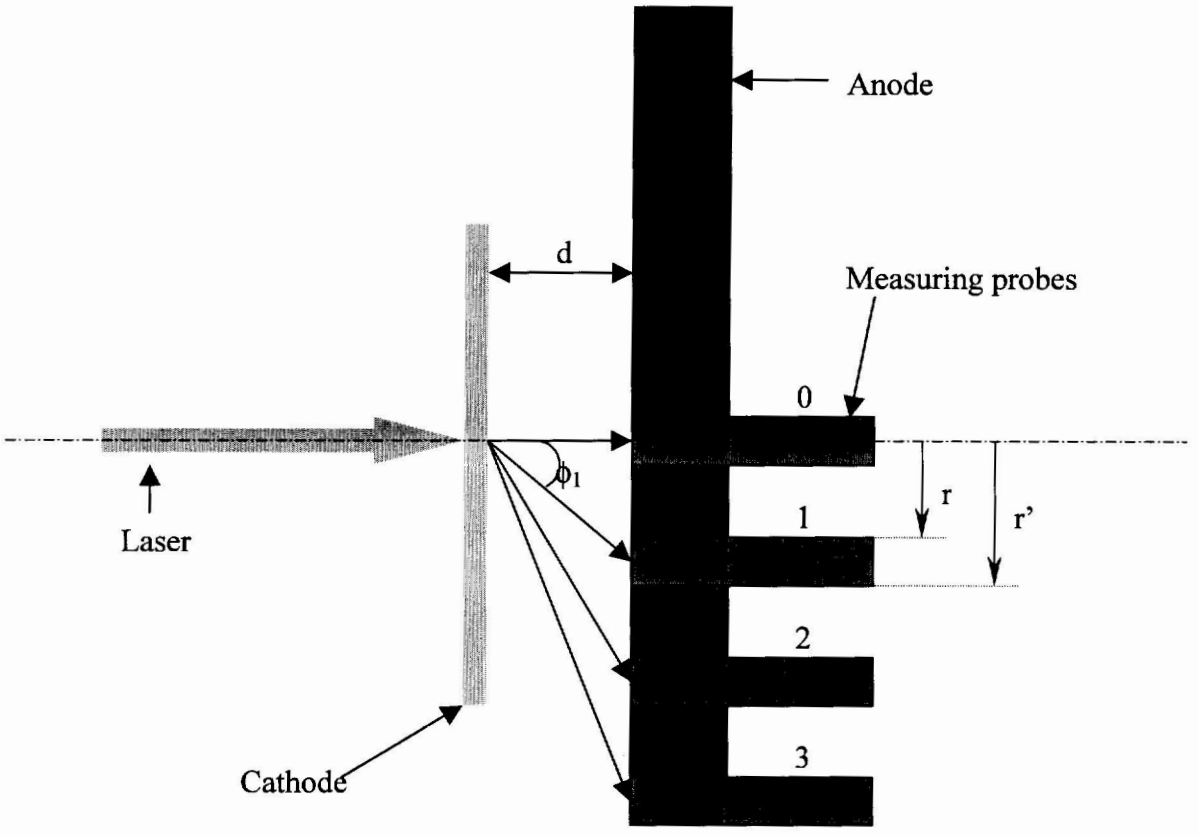

Figure 3.4 Experimental set-up for photoemission angular distribution measurement.

Summary

Two fundamental photoemission properties of a thin-film of gold--energy distribution curve (EDC) and angular distribution curve (ADC)--have been modeled using the three-step model. Experimental measurements were carried out and compared with the theoretical model. A good agreement was found between the theoretical and experimental results. Thus, the model can be used to calculate the I-V characteristics of thin-film gated photocathodes.

References

[1] H.P. Bonzel and CH. Kleint, "On the history of photoemission," Progress in Surface Science, **49**, pp. 107-153, 1995.

[2] R. H. Fowler, "The analysis of photoelectric sensitivity curves for clean metals at various temperature," Phys. Rev. **38**, pp. 45-56, 1931.

[3] L. A. DuBridge, "A further experimental test of Fowler's theory of photoelectric emission," Phys. Rev. **39**, pp. 108-118, 1932,

[4] W. E. Spicer, Photoelectric Emission, in Optical Properties of Solids, Ed. By F. Abeles, North-Holland Publishing Company, p. 755, 1972.

[5] W. E. Spicer, "Photoemissive, photoconductive, and optical absorption studies of alkali-antimony compounds," Phys. Rev. **112**, pp. 114-122, 1958.

[6] C. N. Berglund and W. E. Spicer, "Photoemission studies of copper and silver: theory," Phys. Rev. **136** A, pp. 1030-1044, 1964.

[7] C. N. Berglund and W. E. Spicer, "Photoemission studies of copper and silver: experiment," Phys. Rev. **136** A, pp. 1044-1064, 1964.

[8] W. E. Spicer, "The electronic structure of crystalline solids and photoemission spectroscopy: from Einstein to high temperature superconductors," J. Phys. Chem. Solids, **59**, pp. 527-552, 1998.

[9] W. E. Spicer, "Modern theory and applications of photocathodes," in Photodetectors and Power Meters, Proceedings of SPIE, Vol. 2022, San Diego, CA, Jul. 15-16, pp. 18-33, 1993.

[10] A. H. Sommer, "Brief history of photoemissive materials," in Photodetectors and Power Meters, Proceedings of SPIE, Vol. 2022, San Diego, CA, Jul. 15-16, pp. 2-17, 1993.

[11] A. Herrera-Gomes and W. E. Spicer, "Physics of high intensity nanosecond electron source," in Photodetectors and power meters, Proceedings of SPIE, vol. 2022, San Diego, CA, Jul. 15-16, pp. 51-63, 1993.

[12] X. Jiang, et al. "Photoemission from gold thin films for application in multiphotocathode arrays for electron beam lithography," J. Vac. Sci. Technol. B **16**, pp. 3374-3379, 1998.

[13] C. Neil Berglund, 1999 Annual report: system-level and architectural considerations of multi-electron-beam lithography, Etec Systems, Inc. Hayward, CA..

[14] C. Lee, "High current density photoemissive electron source," Appl. Phys. Lett. **44**, pp. 565-566, 1984.

[15] J. E. Schneider et al., "Patterned nagative electron affinity photocathodes for maskless electron beam lithography," J. Vac. Sci. Technol. B **16**, pp. 3192-3196, 1998.

[16] J. E. Schneider et al. "Semiconductor on glass photocathodes as high-performance sources for parallel electron beam lithography," J. Vac. Sci. Technol. B **14**, pp. 3287-3786, 1998.

[17] A. W. Baum, J. E. Schneider, R. F. W. Pease, M. A. McCord, and W. E. Spicer, " Semiconductor on glass photocathodes for high throughput maskless electron beam lithography," J. Vac. Sci. Technol. B **15,** pp. 2707-2712, 1997.

[18] P. Sen et al., "Lifetime and reliability results for a negative electron affinity photocathode in a demountable vacuum system," J. Vac. Sci. Technol. B **16**, pp. 3380-3384, 1998.

[19] T. Srinivasan-Rao, J. Fischer, and T. Tsang, "Photoemission studies on metals using picosecond ultraviolet laser pulse," J. Appl. Phys. **69,** pp. 3291-3296, 1991.

[20] S. D. Moustaizis, M. Tatarakis, C. Kalpouzos, and C. Fotakis, "High current and directional electron beams produced from gold photocathodes by ultrashort excimer laser pulse," Appl. Phys. Lett. **60**, pp.1939-1941, 1992.

[21] Gy. Farkas, Z. Gy. Horvath, and Cs. Toth, "Linear surface photoelectric effect of gold in intense laser field as a possible high-current electron source," J. Appl. Phys. **62**, pp. 4545-4547, 1987.

[22] D. Charalambidis, E. Hontzopoulos, and C. Fotakis, "High current, small divergence electron beams produced by laser-induced surface photoelectric effect," J. Appl. Phys. **65,** pp. 2843-2846, 1989.

[23] J. P. Girardeau-Montaut, C. Girardeau-Montaut, S. D. Moustaizis and C. Fotakis, "High current density produced by femtosecond nonlinear single-photon photoelectric emission from gold," Appl. Phys. Lett., **62**, pp. 426-428, 1993.

[24] S. Gosavi et al. "Practical gold thin-film photocathodes for advanced electron beam lithography," Symposium on Photomask Technology, Proceedings of SPIE, Vol. 3837, Monterey, CA, September, pp. 501-512, 1999.

[25] W. Pong, R. Sumida, and G. Moore, "Attenuation length for photoelectrons in metal films," J. of Appl. Phys, **41**, pp. 1869-1870, 1970.

[26] R. E. Thomas, "Interference effects in the reflection of low-energy electrons from thin films of Au on Ir," J. of Appl. Phys, **41**, pp. 5330-5334, 1970.

[27] W. Pong, H.K. Nishihara, and D. Chan, "Effect of boundary scattering on photoemission from thin films," J. of the Optical Society of America, **62**, pp. 487-490, 1972.

[28] W. F. Krolikowski and W. E. Spicer, "Photoemission studies of the noble metals. I. Copper," Phys. Rev., **185**, pp. 882-900, 1969.

[29] R. J. Maurer, "Photoelectric Effect," in Handbook of Physics, Ed. by E. U. Condon and H. Odishaw, McGraw-Hill Book Company, New York, p. 67, 1958-1967.

[30] W. F. Krolikowski and W. E. Spicer, "Photoemission studies of the noble metals. II. Gold," Phys. Rev., B **1**, pp. 478-487, 1970.

[31] S. M. Sze, J. L. Moll and T. Sugano, "Range-energy relation of hot electros in gold," Solid-State Electronics, **7**, pp. 509-523, 1964.

[32] L. B. Leder and J. A. Simpson, "Improved electrical differentiation of retarding potential measurements," Rev. Sci. Instrum., **29**, pp. 571-574, 1958.

[33] W. E. Spicer, and C. N. Berglund, "Measurement of photoemitted electron energy distributions by an ac method," Rev. Sci. Instrum., **35**, pp. 1665-1667, 1964.

[34] R. Nathan and C. H. B. Mee, "AC methods for the determination of photoelectron energy distributions," Rev. Sci. Instrum., **38**, pp. 1783-1785, 1967.

[35] T. H. Disefano and D. T. Pierce, "Energy resolution of the photoemission analyzer" Rev. Sci. Instrum., **41**, pp. 180-188, 1970.

[36] F. Pauty, G. Matula, and P. J. Vernier, " An electron spectrometer for measuring both angular and energy distributions of photoemitted electrons" Rev. Sci. Instrum., **45,** pp. 1203-1207, 1974.

[37] W. McMahon and L. Heroux, " Measurement of energy and angular distribution of extreme ultraviolet photoelectrons" Applied Optics, **13**, pp. 438-443, 1974.

[38] R. T. Poole, R, C. G. Leckey, J. G. Jenikin and J. Liesegang, " Photoelectron angular distribution from gold" J. of Electron Spectroscopy and Related Phenomena, **1**, pp. 371-376, 1972/1973.

[39] H. Moss, Chapter 3, "The angular distribution of current from the triode," in Narrow Angle Electron Guns and Cathode Ray Tubes, Ed. By L Marton, Academic Press, New York, pp. 25-39, 1968.

Chapter 4
Theory of Thin-Film Gated Photocathodes

The thin-film gated photocathodes is a novel approach for electron-beam lithography [1]. The similar triode structure has been used for a field emitter [2-4] with a thin-film (0.4 μm) of molybdenum as the gate, with a diameter of 1.5 μm, and a molybdenum cone as the cathode. When a high voltage (>100 volts) was applied to the gate, a high field was formed and electrons were emitted from the cathode.

The arrays constructed by field-emitters were used primarily for vacuum microelectronics [5,6]. Field-emission arrays were also used for flat-panel displays in so-called field-emission displays (FED) [7-9]. More recently, field emission arrays were investigated for electron beam lithography applications [10]. In this instance, the structure studied was a two-dimensional array of miniature planar field emission cathodes consisting of a low electron affinity coating deposited on aluminum biasing pads controlled by CMOS circuitry. Each cathode was individually addressable, providing a matrix of massively parallel but independent electron beams.

The thin-film gated photocathodes, however, differ from the thin-film field emitters fundamentally: (1) The gate in the field emitter creates a high electric field necessary for field emission, whereas the gate in the gated photocathode creates a potential barrier to prevent the photocathode emission; (2) The emission current from the field emitter is a strong function of the gate voltage due to its field emission characteristics, whereas the emission current from a gated photocathode weakly depends

on the gate voltage. Because of these differences, there is little analogy between the two devices despite the structural similarity.

A theoretical study of thin-film gated photocathodes is presented in this chapter. The objectives of this study are to understand the operational principles of gated photocathodes and to provide a theoretical basis for characterization. The principles of operation are first addressed. A theoretical model of the thin-film gated photocathodes is then developed to calculate I-V characteristics. Finally, I-V curves have been simulated as a function of accelerating field, gate diameter and insulator thickness.

4.1 Operation principles of thin-film gated photocathodes

As shown in Figure 1.1, the photoemission region of the thin-film gated photocathode was defined by holes made through the film stack comprising the gate metal, the insulator and the cathode metal. The photocathode material is a thin gold film with a thickness of 15 nm. The diameter of the holes, d, and the thickness of insulator, t, are on a micrometer scale (1-2 μm). A CW UV laser with a wavelength of 257 nm illuminated the photoemission region through the sapphire substrate. The photoelectrons from the photocathode were modulated by the gate with a potential, V_g. The electrons emitted from the gated photocathodes form a beam and are accelerated by the electric field, E_2, between the gate and an anode.

In operation, an anode constructed by an aperture or lens at a high positive potential is set some distance away from the photocathode to accelerate and collect the emitted electrons. If a negative voltage, V_g, with respect to the photocathode is applied to the gate, a potential barrier will be created above the photocathode between the photoemitter and the gate. The magnitude and shape of this potential barrier depends on the insulator thickness, the diameter of the hole in the gate, the accelerating field, and the gate voltage. Photoemitted electrons will be prevented from reaching the anode when this potential barrier height equals the maximum energy of the photoemitted

electrons. The gate voltage to set up this condition is defined as the extinction voltage, V_x. With increases in gate voltage starting from V_x, the potential barrier decreases and electrons can be emitted from the gated photocathode. Eventually, the potential barrier will disappear, and electrons of all energy levels reach the anode. Due to the angular distribution of the photoemission, some electrons will hit the insulator, some will be collected by gate and most of the electrons will be collected by anode. The current components are functions of the gate voltage for a given accelerating field and dimension of the gated photocathode.

If the insulator is idealized in the sense that no charging effects within it or on its surface are assumed to occur during illumination of the structure, the cathode, I_c, gate current, I_g, and anode current (or beam current), I_a, have the relationship:

$$I_c = I_g + I_a \qquad (4.1)$$

i.e. the cathode current is equal to the sum of the gate current and anode current, which satisfies Kirckhoff's Law.

4.2 Current-voltage (I-V) characteristics

4.2.1 Extinction gate voltage

Because the purpose of the gate is to electrically turn off the photoemission, the extinction gate voltage is one of the most important parameters. As described in the previous section, when the gate voltage is more negative than the extinction voltage, the potential minimum is higher than the maximum electron energy. Thus no electron can surpass the barrier, and the current falls to zero. The condition can be quantitatively described as,

$$q\Psi(r=0,z)\,|_{d\Psi/dz=0} = E_{\max} \qquad (4.2)$$

where r is the radius, z is the axis normal to the photocathode plane, r and z originate at the center of gate, $\Psi(r,z)$ is the potential, and E_{max} is the maximum energy of the photoemission. From Equation (3.1), E_{max}, is 0.6 eV for a photon energy of 4.89 eV and a work function of 4.3 eV. An approximate analytical solution of the electrical field in Reference [11] was applicable to the structure studied in this investigation with the assumptions: (1) Far away from the cathode, the accelerating field, E_2 is uniform; (2) The thickness of the gate is infinitely small.

For a given accelerating field, gate diameter, and insulator thickness, the extinction gate voltage can be calculated numerically by satisfying equation (4.2). The curves in Figure 4.1a are calculations of the extinction gate voltage as a function of E_2 for several geometric configurations, which shows that the extinction gate voltage is a strong function of gate diameter and accelerating field. The curves in Figure 4.1b are the calculated extinction gate voltage for a gated photocathode with d = 2 μm, t = 2 μm, for different E_{max}. These curves represent the case where a different photocathode material with a different work function is used. Extinction gate voltage shifts proportionally to E_{max}. From these calculations, it is apparent that the beam current can be turned off with only several volts applied on the gate, even for a high accelerating field.

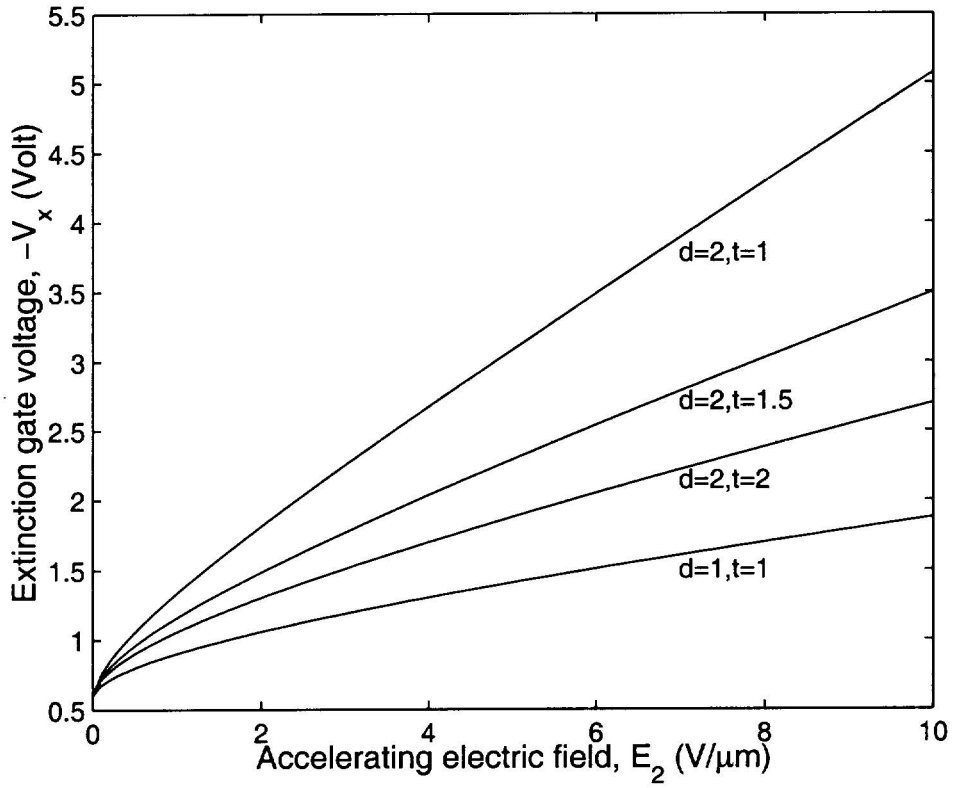

Figure 4.1a Computed extinction gate voltage, V_x, as a function of accelerating electric field, E_2, for different gate diameter, d, and insulator thickness, t [1].

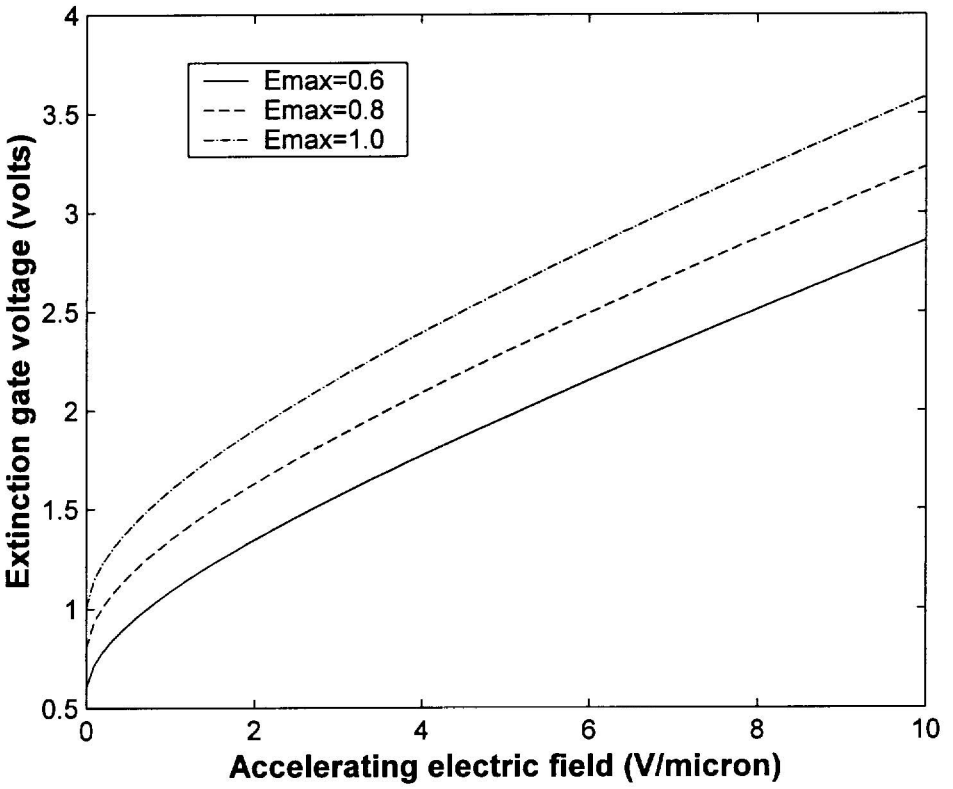

Figure 4.1b Computed extinction gate voltage, V_x, as a function of accelerating electric field, E_2, with d = 2 μm, t = 2 μm for different E_{max} (eV).

4.2.2 I-V characteristics

Photoemission from a photocathode is a function of both the energy distribution curve and the angular distribution curve:

$$I = \int_A dA \int_{E_i}^{E_{max}} \eta(E, h\nu) dE \int_0^{\phi_j} H(\phi) d\phi \qquad (4.3)$$

where A is the total photocathode emission area of photocathode, E_i is the potential barrier, E_{max} is the maximum energy of photoelectrons equal to the total energy spread, $\eta(E,h\nu)$ is the energy distribution curve (EDC) defined by Equation (3.20), ϕ_j is the emission angle for a certain energy level, E_j, and $H(\phi)$ is the angular distribution curve (ADC) defined by Equation (3.32). With a known energy distribution, $\eta(E, h\nu)$, and angular distribution, $H(\phi)$, the major task is then to find out the potential barrier, E_i, and the emission angles corresponding to the energy levels from E_i to E_{max}, ϕ_j, for a given electric field and dimensions.

For a non-uniform field, there is no explicit relationship between E_j and ϕ_j. The emission angle can be calculated by a ray tracing method. Ray tracing was done numerically using the method described in Reference [12]. Besides the assumption made in 4.2.1, the current intensity is assumed to be very small and the space charge effect is not considered for. Using this method, the trajectory path of one electron with an initial velocity at an initial position was calculated in a time domain. Examples of the trajectory were studied in detail for the electrons with initial energy of 0.6 eV emitted from the structure with a gate diameter, d = 2 μm, and an insulator thickness of insulator, t = 2 μm, under the accelerating field of E_2 = -0.5V/μm and various gate voltages. The increase of the angle is 3 degrees. Figure 4.2a shows the trajectory path of electrons emitted from the center (z = -2 μm, r = 0 μm) for a gate voltage, V_g = -0.5V (only half was plotted due to the symmetry in this point). Figure 4.2b shows the same

case of Figure 4.2a except $V_g = 0.5V$. Figure 4.2c shows the trajectory from the position of z = -2 μm and r = 0.5 μm with $V_g = -0.5V$, similarly Figure 4.2d shows the trajectory for $V_g = 0.5V$. Comparing Figure 4.2a, Figure 4.2c, for $V_g = -0.5V$, with Figure 4.2b, Figure 4.2d, for $V_g = 0.5V$, respectively, it is apparent that more electrons (or a larger emission angles) emitted for a higher gate voltage.

By this way, the emission angle for an individual energy level can be calculated. Figure 4.3 shows ϕ_j as a function of E_j and V_g. It is apparent that only the high energy electrons are emitted when the gate voltage is negative. Also the low energy electrons have bigger emission angles for a positive gate voltage.

Figure 4.4 is a two-dimensional (2D) diagram of the electron emission path from one gated photocathode. For every position, except the center of the photoemission area, there are four angles corresponding to one electron energy level: $\phi_{c,1}$, $\phi_{c,2}$ (the maximum emission angles of electrons emitted from photocathode), $\phi_{g,1}$, $\phi_{g,2}$ (the maximum emission angle of electron emitted from gated photocathode). Emission in the cone constructed by $\phi_{g,1}$ and $\phi_{g,2}$ contributes to the anode current, I_a, and that of $\phi_{c,1}$ and $\phi_{c,2}$, the cathode current, I_c. The difference between I_c and I_a is the gate current, I_g. To calculate the number of the electrons in this non-symmetrical cone, an effective emission angle is introduced, ϕ_{effect}, which can be defined as,

$$\phi_{effect} = \phi_2 + f(\phi_1 - \phi_2) \qquad (4.4)$$

where f is a fractional factor and expected to be a function of the position and geometry of the gated photocathode. In this simulation, f is set to be a uniform factor of 0.4-0.6.

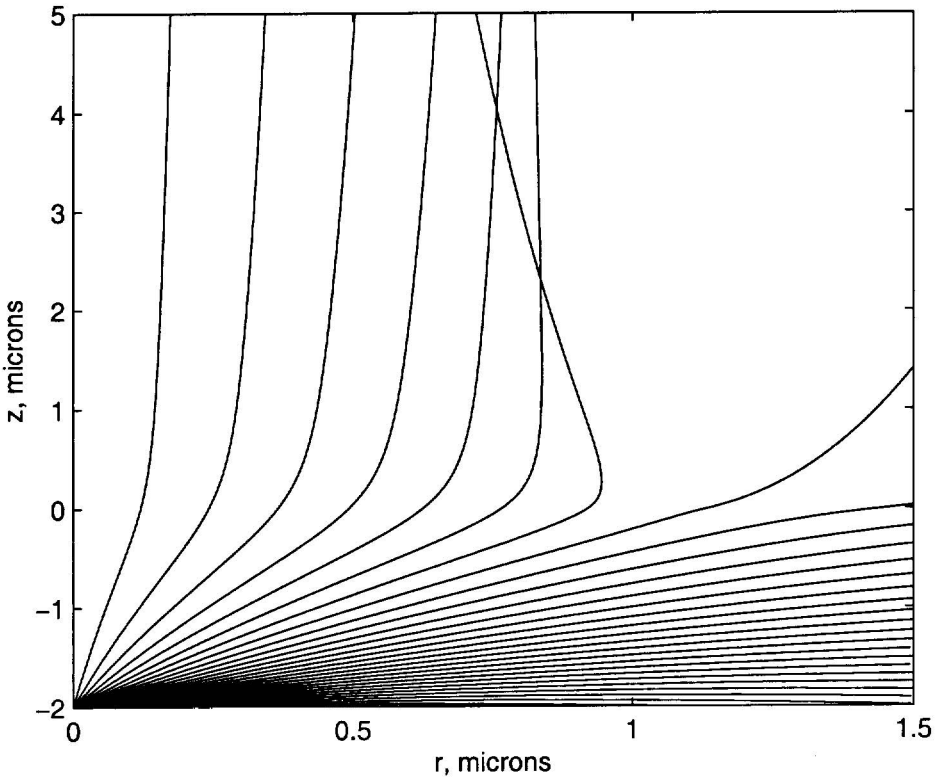

Figure 4.2a Trajectory path of electrons with initial energy of 0.6 eV emitted from the center (z = -2 μm, r = 0 μm) for a gate voltage, V_g= -0.5V and E_2 = -0.5 V/μm (only half was plotted due to the symmetry in this point).

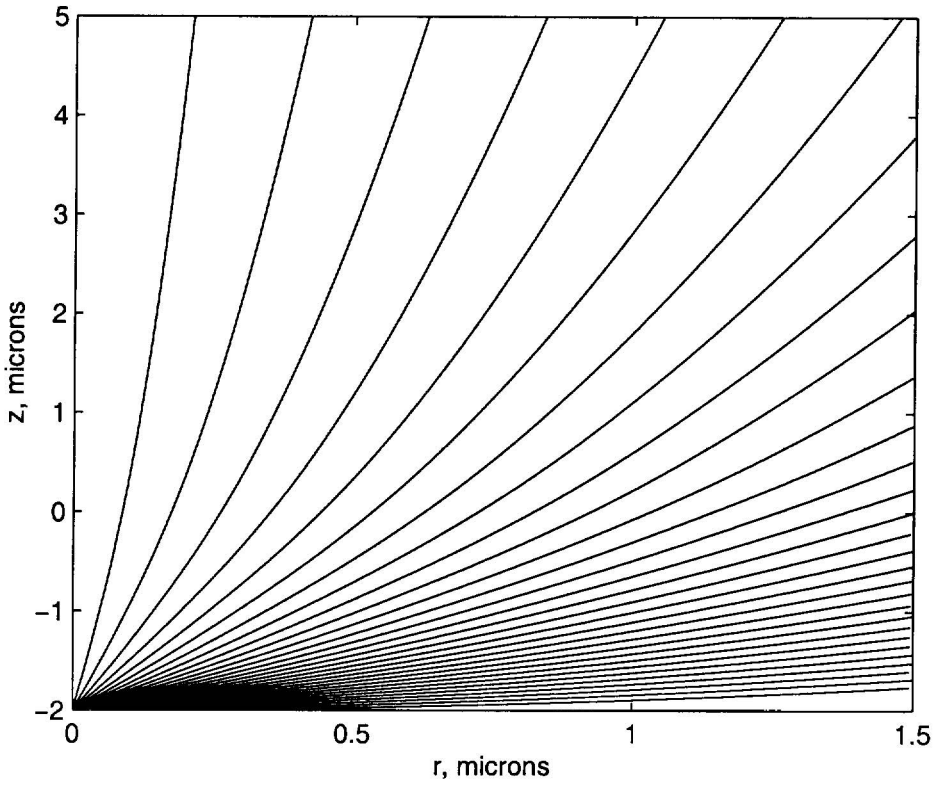

Figure 4.2b Trajectory path of electrons with initial energy of 0.6 eV emitted from the center (z = -2 μm, r = 0 μm) for a gate voltage, V_g = 0.5V, and an accelerating field, E_2 = -0.5 V/μm (only half was plotted due to the symmetry in this point).

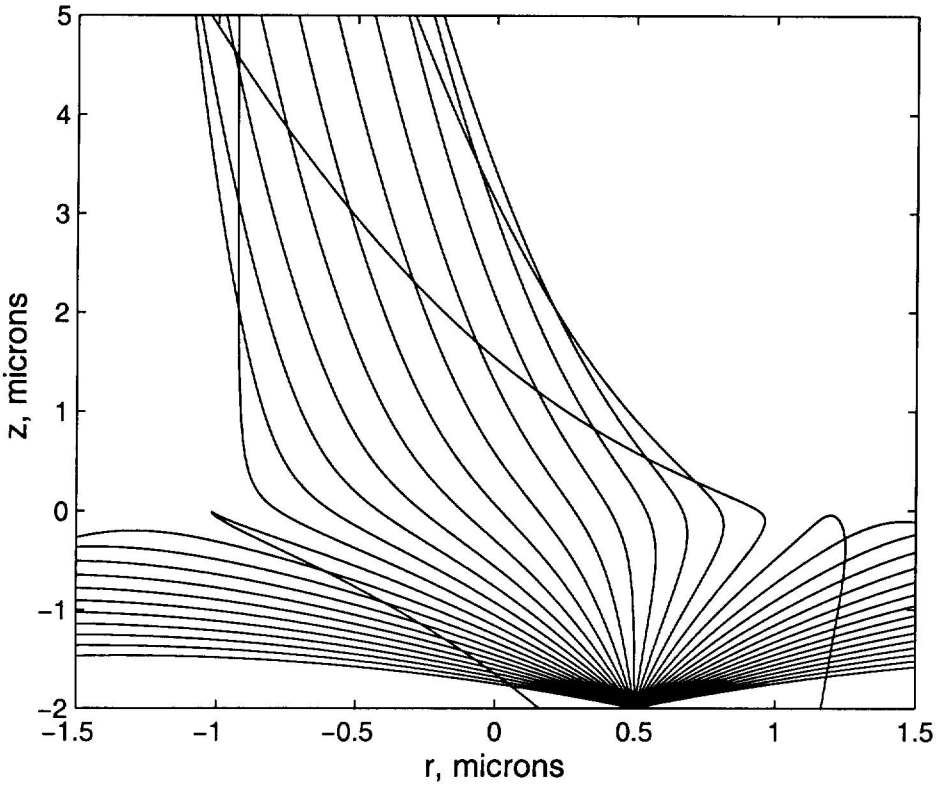

Figure 4.2c Trajectory path of electrons with initial energy of 0.6 eV emitted from the position of z = -2 μm, r = 0.5 μm for a gate voltage, V_g = - 0.5V, and an accelerating field, E_2 = -0.5 V/μm.

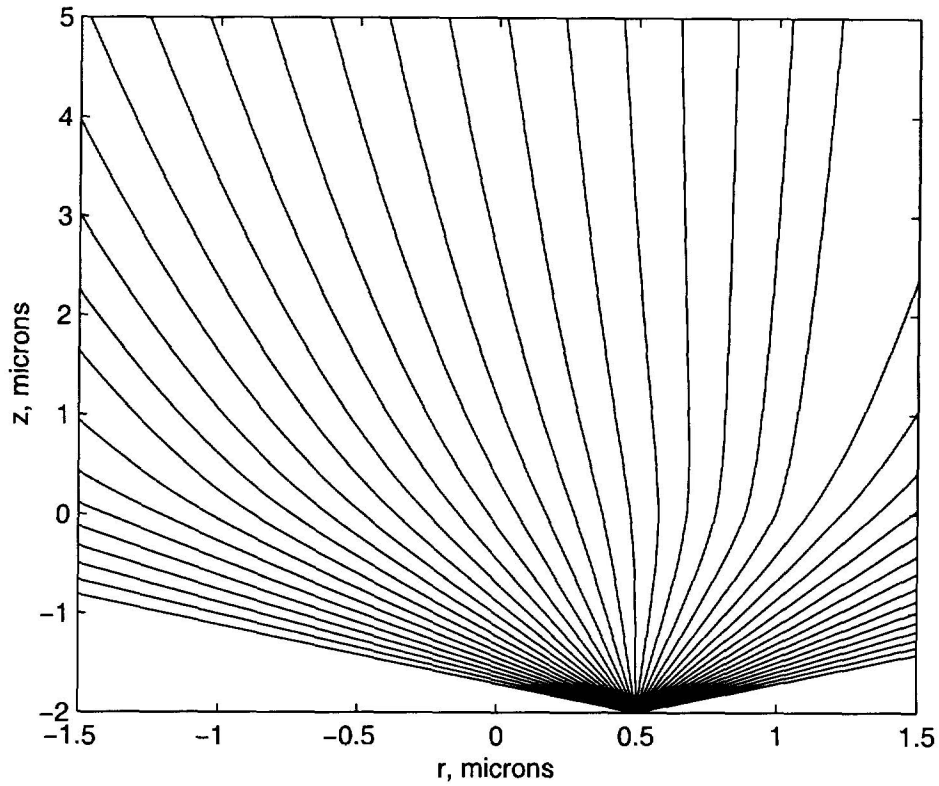

Figure 4.2d Trajectory path of electrons with initial energy of 0.6 eV emitted from the position of z = -2 μm, r = 0.5 μm for a gate voltage, V_g = 0.5V, and an accelerating field, E_2 = -0.5 V/μm.

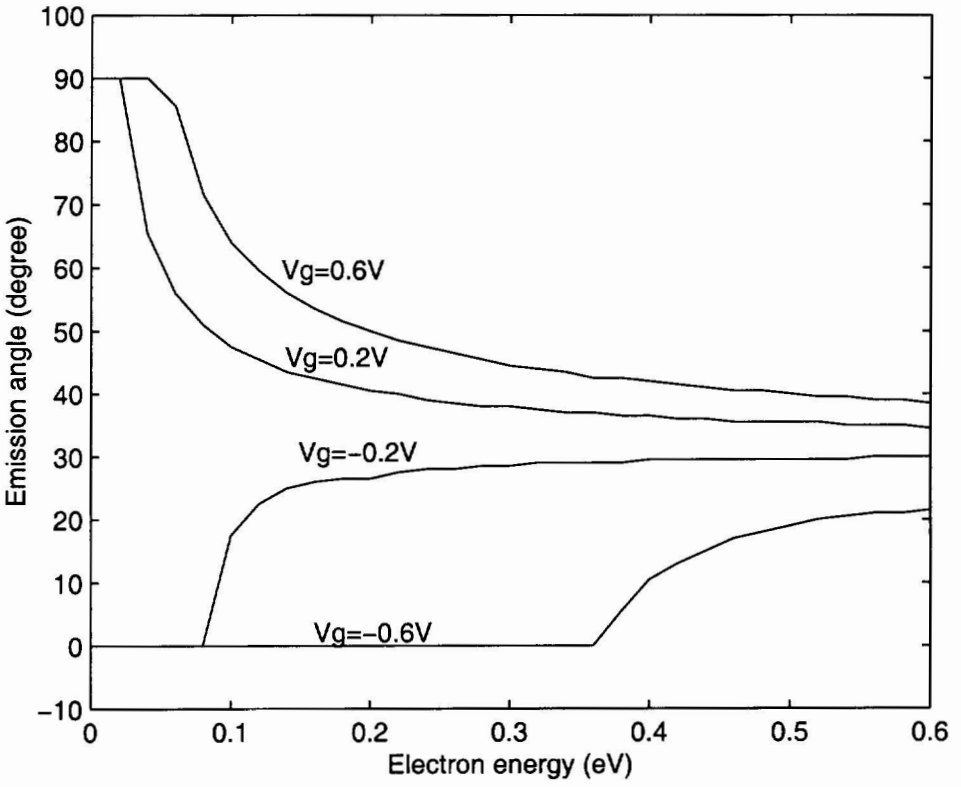

Figure 4.3 Emission angle ϕ_j as a function of E_j and V_g for an accelerating field, E_2 = -0.5 V/μm.

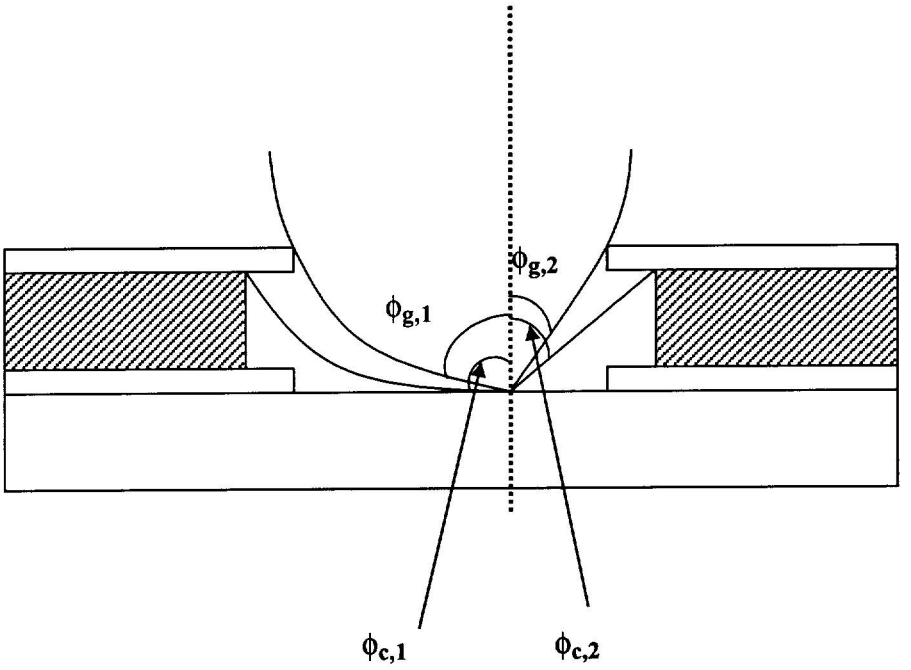

Figure 4.4 2D diagram of the electron emission path from one gated photocathode. The effective emission angle can be calculated as $\phi_{effect} = \phi_2 + f(\phi_1 - \phi_2)$.

4.2.3 Modeling the Schottky effect

The calculated current-voltage characteristics generally fit with the experimental results, except for over the high gate voltage region where the calculated slope is very small compared with the experimental results. Note that the thickness of the insulator is on the micrometer scale. Even with a few volts applied to the gate, the electric field between the gate and the cathode can be high. The barrier lowering due to the image charge in a high field is known as the Schottky effect:

$$\Delta\Phi = \sqrt{\frac{q\xi}{4\pi\varepsilon_0}} \qquad (4.5)$$

where $\Delta\Phi$ is the barrier lowering, ξ is the electrical field on the surface, and ε_0 is the vacuum permittivity.

Photoemission is strongly dependent on the work function, and any small change of the work function can cause a large change in the photocurrent. The Schottky effect on the photoemission has been experimentally observed [13]. The Schottky effect is taken into account for the I-V calculation by calibration of the work function for every point. Figure 4.5 shows the calculated I-V curves with the Schottky effect compared with that of no Schottky effect. I-V curves with the Schottky effect overlap those without the Schottky effect in region I and II. In region III, the cathode current shows a positive slope, or increases with the gate voltage.

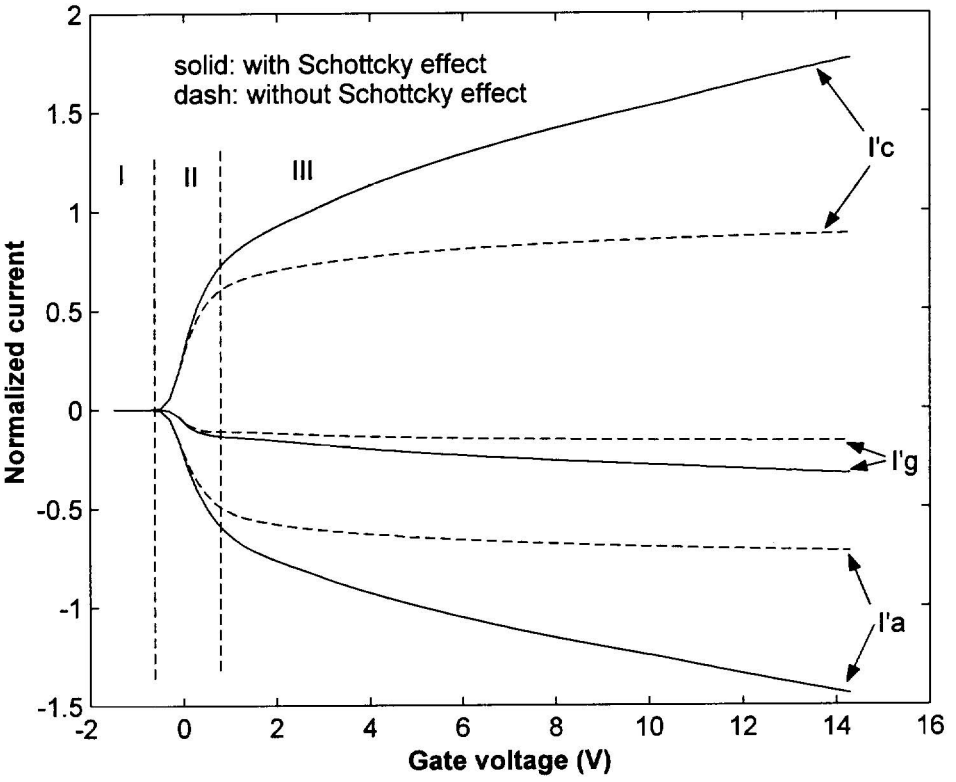

Figure 4.5 Calculated I-V characteristics as a function of the presence of the Schottky effect. The curves were normalized by the saturated photocurrent from the same photoemission area without Schottky effect.

4.2.4 Interpreting the simulated I-V characteristics

Simulated I-V characteristics with the addition of the Schottky effect in Figure 4.5 reflect the typical current-voltage characteristics. These curves are normalized by the saturated photocurrent from the same photoemission area without the Schottky effect. The normalized I-V curves depend only on the photocathode configuration and electric fields (not the quantum efficiency). The normalized I-V curves can be used to predict the beam current of a given photocathode with known quantum efficiency. The cathode current, I_c, (or anode current, I_a) can be clearly divided into three regions, region I for which I_c is 0, region II of bigger slope, region III of smaller slope. The gate voltage for $I_c = 0$ is defined as the extinction gate voltage, which has been addressed, in detail, in Section 4.2.1. In this region, the potential barrier formed by the negative gate voltage is bigger than the maximum energy of the photoelectrons, no electrons can emit from the photocathode. In region II, the potential minimum is reduced and the electrons with an energy higher than the potential barrier will escape. The beam current was dominated by the energy spread of the photoemission, yet also depends on the emission angle. This region was defined as the gate voltage modulation region, i.e. the energy spread (the difference of the maximum electron energy and the minimum electron energy) of the emitted electrons is a function of the gate voltage. In region III, the potential barrier formed by the negative gate voltage no longer exists, electrons in every energy level can emit. The beam current depends on the gate voltage, i.e. the current increases with the gate voltage. The positive slope in this region is mainly due to the work function lowering, the Schottky effect. Larger angle electrons also contribute to this slope but much less than the Schottky effect. It should be pointed out that, starting from a certain gate voltage, the normalized cathode current is bigger than unity due to the Schottky effect, which can be defined as the photoemission enhancement of the gated photocathode.

For the ideal case, as assumed before, the cathode current is equal to the summation of the beam current and gate current. When the gate voltage is negative, nearly no electron was collected by the gate, and therefore the gate current is zero. When the gate voltage becomes positive, the gate current is still much smaller than the beam current. This can be explained by analyzing the origins of the gate current: (1) Photoemission in high emission angles that 'hit' the gate and are collected; (2) Electrons with low momentum in the normal direction that are attracted by the fringing field created due to the thickness of the gate. When the gate thickness is insignificant, the lateral field is confined to a small region. With a high gate voltage, the electrons gain energy in the vertical direction and form a paraxial ray, and thus are less likely to be collected by the gate. When the gate voltage becomes infinitely bigger, nearly all of the electrons tend to be pulled out and the gate current will fall to zero again. In this case, the beam current tends to equal the cathode current.

4.3 Simulation results

In this section, the model developed in section 4.2 was used to simulate the I-V relationship as a function of E_2, d, t and the ratio of d/t. The gate diameter and the insulation layer thickness are in micrometer or sub-micrometer scale in this simulation, which are expected to be the practical gated photocathode configurations. The accelerating field of 10 V/μm is the desired electric field used for EBL systems. The gate voltage is set from –2 V to 12 V, matching with the range used in the experimental study in next chapter, and the extrapolation to a high gate voltage is not a problem. The extinction gate voltage, V_x, the slopes in region II and III, and the magnitude of the currents are the major characteristics of the I-V curves.

The effect of E_2 was simulated as shown in Figure 4.6. I-V curves were calculated for a range of accelerating fields, E_2 = 0.1, 1, 5 and 10 V/μm from a gated

photocathode with a gate diameter of 1 μm and an insulator thickness of 0.5 μm. The lower limit of the accelerating field used in this simulation is the field used in the experiment in next chapter, the upper limit of the accelerating field is 10 V/μm, and the increase step is set arbitrarily. The I-V curves shift almost parallel to the direction of negative gate voltage with increase of the accelerating field. A large accelerating field has two impacts on the I-V characteristics: (1) It results in a more negative extinction gate voltage which needs to compete with the accelerating field, E_2, to create a potential barrier equal to the maximum energy of photoemission; (2) It results in a smaller I_g; a percentage of electrons which would be collected by the gate gain energy in the axial direction and emit from the gated photocathode. The currents depends more strongly on V_g. Figure 4.6 shows that, over a range of V_g, the I-V curves of different E_2 have a uniform slope which is a function of the ratio of d/t.

Figure 4.7 shows the effect of gate diameter, for t = 0.5 μm, and E_2 = 10 V/μm. The extinction gate voltage increases with gate diameter. E_2 is easier to penetrate into the gate area for a bigger gate diameter and thus a higher gate voltage is needed to compete with E_2 to form a big enough potential barrier. The gate diameter has less effect on the slope in region III but a high d/t ratio results in a large slope in region II.

Figure 4.8 shows the effect of insulation layer thickness, for a gated photocathode with gate diameter of 1.0 μm and E_2 = 10 V/μm. The extinction gate voltage weakly depends on the thickness, and increase with the thickness decrease. The slope in region II depends on the ratio of d/t. It is apparent that a decrease in insulator thickness results in a bigger slope in region III. This dependency is actually due to the Schottky effect. The electric field between the gate and cathode increases for a thinner insulator and work function lowering becomes more significant.

Figure 4.9 shows the effect of device scaling. As mentioned in Chapter 2, one of the advantages of thin-film gated photocathodes is that their dimensions, or the beam sizes, can be easily scaled down. Thus, it is desirable to know the effect of scaling on the I-V characteristics. The simulation was conducted for a uniform d/t ratio for d = t =

2.0 μm, d = t = 1.0 μm and d = t = 0.5 μm. The extinction gate voltage increases with the gate diameter. The slop of I-V in region II is almost uniform for three cases. The most significant scaling impact on I-V is in region III, where the slope strongly depends on the insulation layer thickness (which can also be explained by the Schottky effect). Thus it is concluded that thickness of the insulator is the dominant factor in scaling,

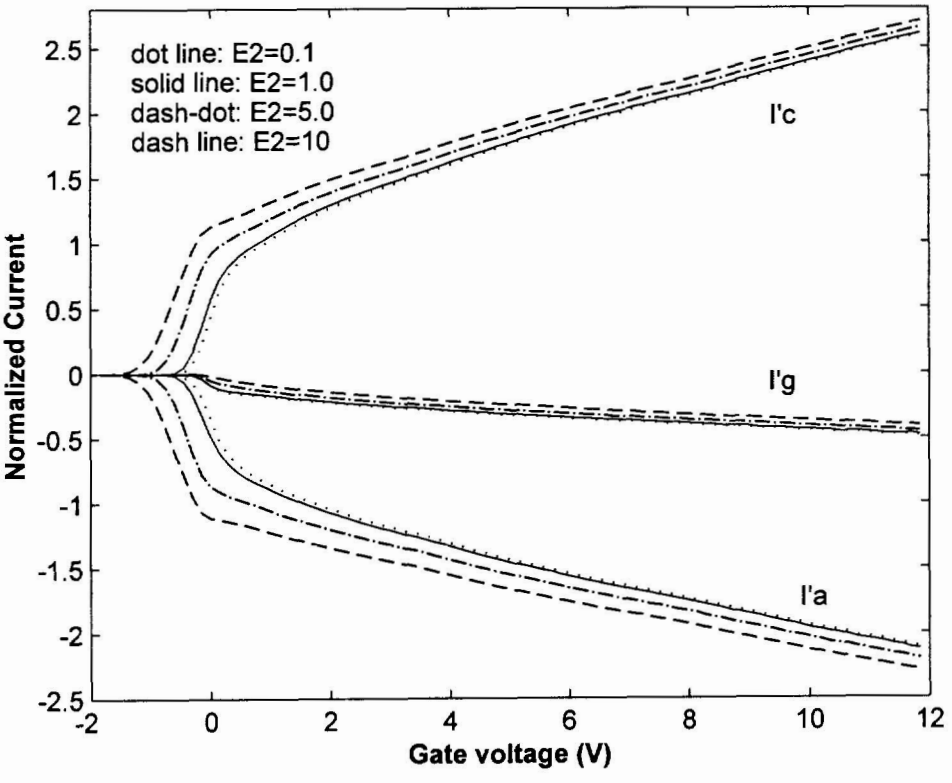

Figure 4.6 Simulated I-V curves of a gated photocathode with a gate diameter of 1 μm and an insulator thickness of 0.5 μm for a range of accelerating fields, E_2 (V/μm).

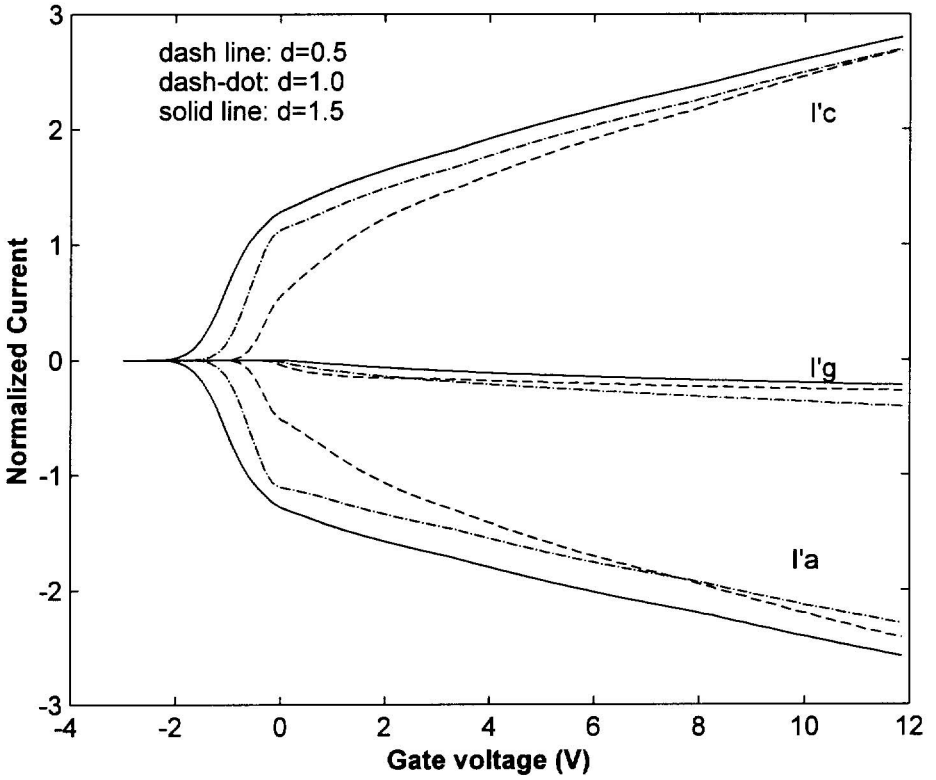

Figure 4.7 Simulations of the effect of gate diameter (d = 0.5, 1.0 and 1.5 μm) for t = 0.5 μm, and E_2 = 10 V/μm.

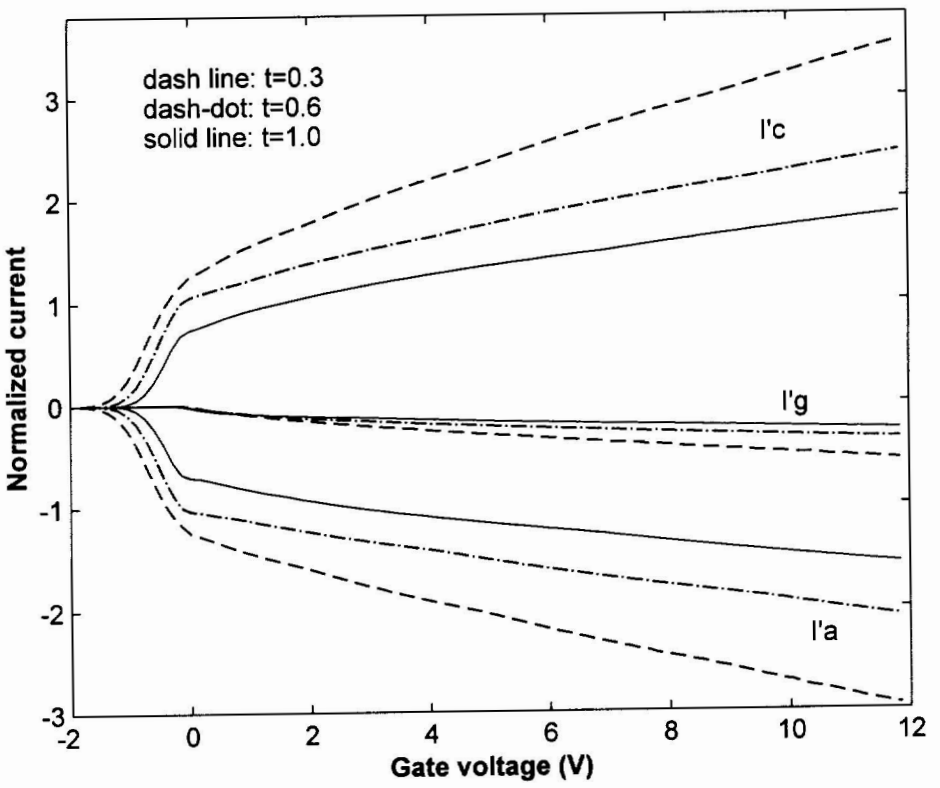

Figure 4.8 Effect of the insulator thickness (t = 0.3, 0.6 and 1.0 μm) for a gated photocathode with a gate diameter of 1.0 μm and E_2 = 10 V/μm.

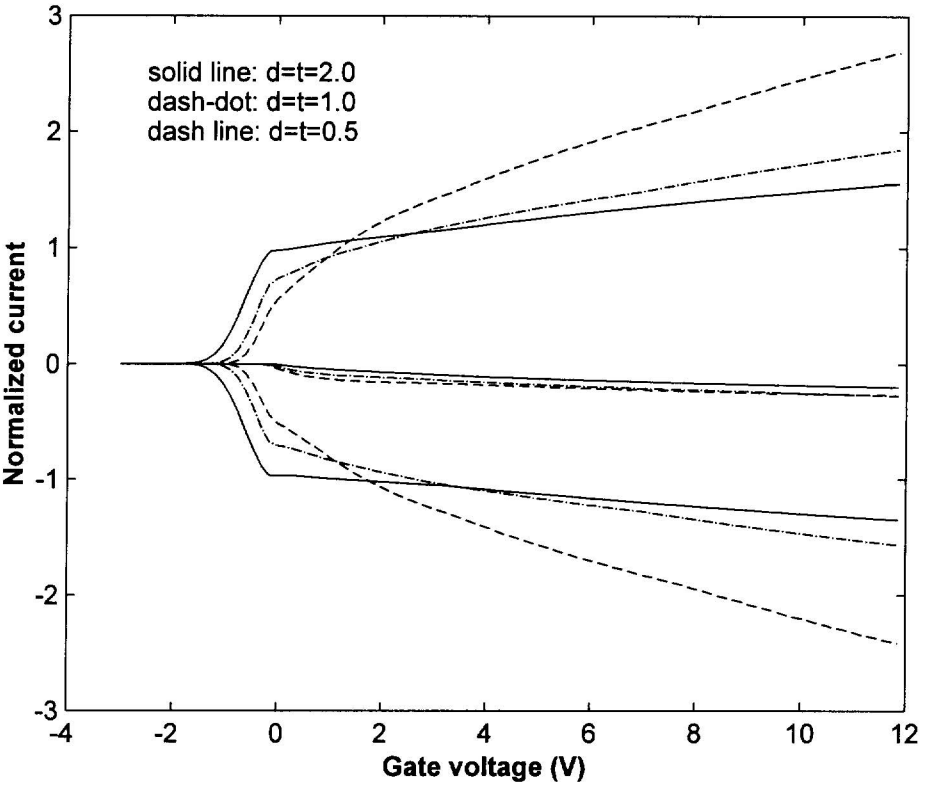

Figure 4.9 Simulating the effects of device scaling on I-V characteristics (dimensions in micrometer scale).

4.4 Discussion

In general, for an ideal case described in section 4.1, i.e. zero gate metal thickness and no space charge effect, the I-V characteristics of the thin-film gated photocathode depend on the electric field in the gate area. The electric field is determined by the gate voltage, V_g, accelerating field, E_2, gate diameter, d, and insulation layer thickness, t. The effects of these factors have been simulated in Section 4.3. In this section, several fundamental concerns are discussed, including, the extinction gate voltage, the gate metal thickness, the gate diameter and the brightness.

The extinction gate voltage is largely determined by E_2 and d. The extinction gate voltage depends less on t. For a gated photocathode in micro-scale, the extinction gate voltage is required to turn off the electron beam for the studied cases is only a few volts, even with a E_2 as high as 10 V/μm; In designing the gate diameter, the extinction gate voltage thus does not pose a restriction on the size of gate.

The gate metal thickness could not be incorporated in the field analysis and therefore the effect of this factor could not be simulated. However, the thinner gate metal results in a smaller fringing field which has less impact on the path of electron. Therefore electrons emitted from photocathode are less likely to be collected by the gate. This impacts the gated photocathode emission efficiency.

The gate diameter is limited by the beamlet size. As discussed in Section 4.2, the emitted electrons are paraxial. The gate diameter can be regarded as the virtual source size for the present thin-film gated photocathode structure. The smaller gate diameter will result in a smaller beamlet size. On the other hand, the diameter of the gate determines the size of the photoemission area. The diameter of the photoemission area is slightly smaller than the gate diameter to guarantee a good contact between the photoemitter and photocathode metal. To obtain enough beam current, the photoemission area has to be big enough to provide the desired beam current.

A potential high beam current source can be obtained by using a high quantum efficiency photoemitter and high power illumination. The beam current may be

improved by the Schottky effect as explained in section 4.2. A thinner insulator and high gate voltage are thus desired.

Summary

The principles of operation of the thin-film gated photocathode were explained by analyzing the electric fields and photoemission properties of the photocathode. I-V characteristics of thin-film gated photocathode were calculated by using theoretical EDC, ADC and ray tracing methods. The models successfully simulated the I-V characteristics of the gate voltage, the accelerating field and the dimensions of the gated photocathode. The models also provide an insight into the emission process of gated photocathodes.

The simplicity of beam modulation can reduce the complexity, improve the reliability, provide the flexibility and add efficiency to the whole lithography system. Due to its high field, thin-film gated photocathodes are expected to deliver higher beam current, better defined electron-beams than conventional photocathodes.

References

[1] Z. Pei, J. McCarthy, C. N. Berglund, T. P. H. Chang, M. Mankos, K. Y. Lee, and M. L. Yu, "Thin-film gated photocathodes for electron-beam lithography," J. Vac. Sci. Technol. B **17**, pp. 2814-2818, 1999.

[2] C. A. Spindt, "A thin-film field-emission cathode," J. Appl. Phys., **39**, pp. 3504-3505, 1968.

[3] C. A. Spindt, I. Brodie, L. Humphrey, and E. R. Westerberg, "Physical properties of thin-film field emission cathodes with molybdenum cones," J. Appl. Phys., **47**, pp. 5248-5263, 1976.

[4] R. E. Neidert, P M. Philips, S. T. Smith, and C. A. Spindt, "Field emission triodes," IEEE Transactions on Electron Devices, **38**, pp. 661-665, 1991.

[5] C. A. Spindt, C. E. Holland, A. R. Rosengreen, and I. Brodie, "Field-emitter arrays for vacuum microelectronics," IEEE Transactions on Electron Devices, **38**, pp. 2355-2363, 1991.

[6] T. Utsumi, "Keynote address, vacuum microelectronics: what's new and exciting," IEEE Transactions on Electron Devices, **38**, pp. 2276-2283, 1998.

[7] W. D. Kesling and C. E. Hunt, "Beam focusing for field-emission flat panel displays," IEEE Transactions on Electron Devices, **42**, pp. 340-346, 1995.

[8] C. Py, J. Itoh, T. Hirano, and S. Kanemaru, "Bean focusing characteristics of silicon microtips with an in-plane lens," IEEE Transactions on Electron Devices, **44**, pp. 498-502, 1997.

[9] T. Ko, B. Chung, J. Y. Lee, and D. Jeon, "Fabrication and simulation of a gated thin film emitter," J. Vac. Sci. Technol. B **16**, pp. 700-704, 1998.

[10] V. I. Merkulov, et al. "An addressable field emission array for e-beam lithography using planar, pulsed-laser deposited amorphous diamond cathodes," Proceedings of the IEEE International Vacuum Microelectronics Conference, Jul. 19-24, 1998, Asheville, NC, pp. 178-79; M. J. Paulus, et al., "Addressable amorphous diamond field emission array for e-beam lithography," Annual Device Research Conference Digest Proceedings of the 1998, Jun. 22-24, 1998 Charlottesville, VA, pp. 122-123.

[11] See, for example, Miklos Szilagyi, Electron and Ion Optics, Plenum Press, New York, p. 77, 1988.

[12] O. Klemperer, Electron Optics, Cambridge University Press, p. 473, 1971.

[13] T. Srinivasan-Rao, J. Fischer, and T. Tsang, "Photoemission studies on metals using picosecond ultraviolet laser pulse," J. Appl. Phys. **69**, pp. 3291-3296, 1991.

Chapter 5
Fabrication and Characterization of Thin-Film Gated Photocathodes

The fabrication and characterization of thin-film gated photocathodes is covered in this chapter. The characterization of the thin-film gated photocathodes was motivated to: first, demonstrate the concept of the thin-film gated photocathode by proving its feasibility; and second, explore the factors affecting the I-V curve. Ten thin-film gated photocathodes with different configurations were fabricated, with which the I-V characteristics related parameters have been fully explored.

5.1 Fabrication of thin-film gated photocathodes

Thin-film gated photocathodes as shown in Figure 1.1 were fabricated at the Oregon Graduate Institute. The gated photocathode was built on a sapphire substrate. A gold thin-film with a thickness of 10-15 nm was used as the photocathode which was defined by the cathode metal, a 50 nm thick chromium film. The diameter of the photocathode was 1~3 μm. Another chromium film with a thickness of 70-100 nm was deposited above the photocathode electrically isolated by an insulation layer of silicon oxide with a thickness of 1~2 μm. The fabrication process is shown in Figure 5.1 consisting of four steps: (a) multi-layer thin film stack deposition; (b) patterning by FIB; (c) wet etch to undercut the SiO; (d) and gold film deposition.

The substrate, double-side-polished C-plane (0001) sapphire, has a good light transmission property and excellent thermal conductivity. It was prepared by cleaning using high purity Acetone and Methanol, and dried by compressed air. A 50 nm thick chromium film, a 1-2 μm layer SiO and another 70-100 nm thick chromium film were successively deposited on the substrate by vacuum thermal evaporation at a vacuum in the 10^{-7} Torr range. A tungsten basket was used to heat chromium chunks (0.15-2 mm pieces). Chromium film was deposited at ~1500 °C (melting point, 1900 °C) through sublimitation. The merit of this low temperature process is that the intrinsic stress can be reduced. The deposition speed of chromium is about 4 Å/s.

The insulation layer was also deposited by thermal evaporation. A tungsten boat was used to heat SiO source materials (purity, 99.9%, size, -10 mesh) to a temperature of 1100 °C achieving a deposition speed of ~25 Å/s. The resultant composition is SiO_{1-x} due to the thermal decomposition of SiO. This film, however, has a dielectric property adequate for this investigation. Chromium and SiO were chosen for constructing the gated photocathodes because: (1) They can be deposited by a thermal vacuum evaporator, which was the only available equipment to deposit the films at OGI; (2) The resulting structure is mechanically stable due to the good adhesive property of chromium.

An FEI 610 focused ion beam (FIB) workstation was used to etch the film stack. The FIB uses a Ga-ion beam-capable of etching both metals and dielectrics. Also, the beam size and the shape are well-defined. In this study, a programmable beam with a 750 Å spot size was employed. End-point detection in the FIB allows for precise milling depth control. Holes with diameter of 1-2 μm were then milled through the film stack of Cr/SiO/Cr to expose the underlying sapphire substrate. The FIB milling profile is such that the milled area has a truncated conical profile: the diameter at the bottom is smaller than that of the top (Δd = 0.1-0.2 μm).

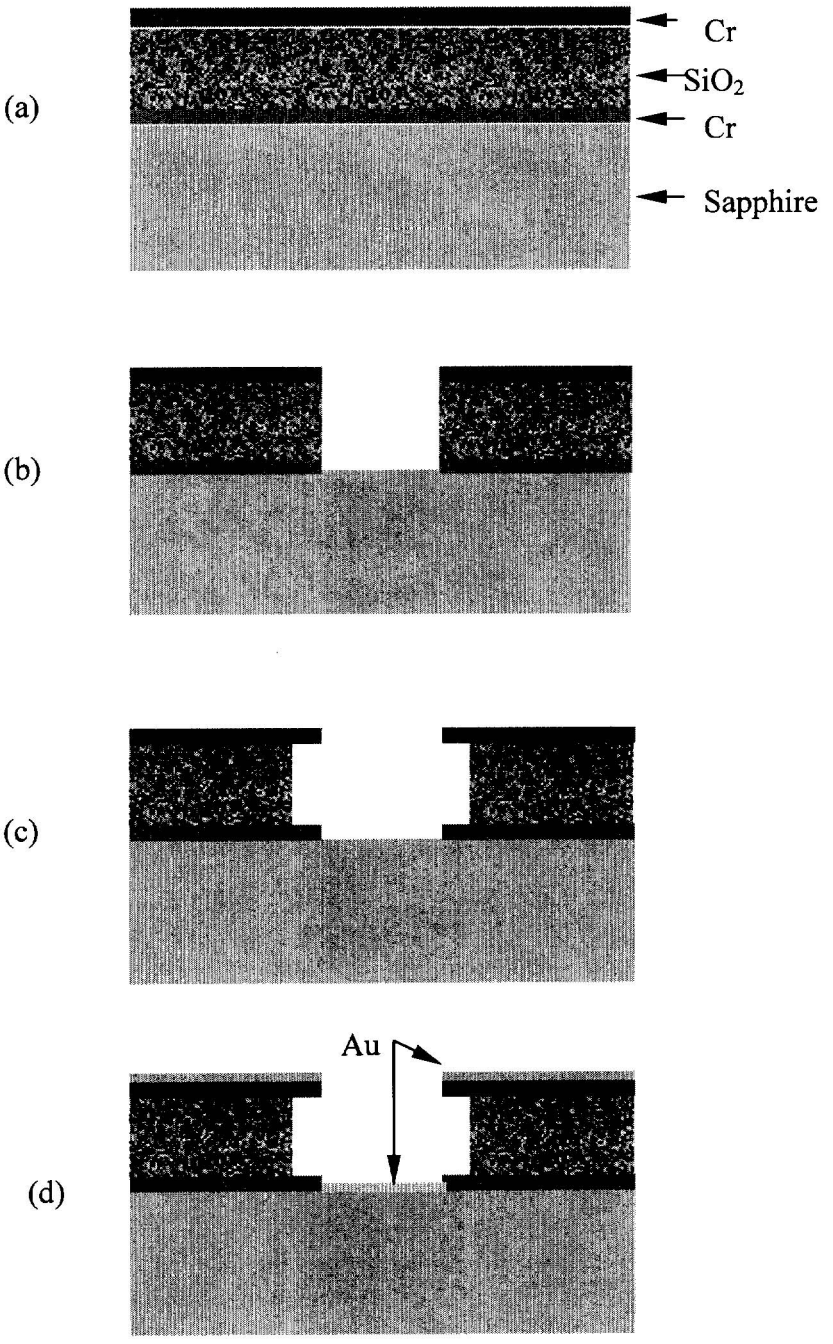

Figure 5.1 Fabrication process of thin-film gated photocathodes (dimension not drawn to scale); (a) film deposition; (b) patterning by FIB; (c) wet etch to undercut the SiO; (d) gold film deposition.

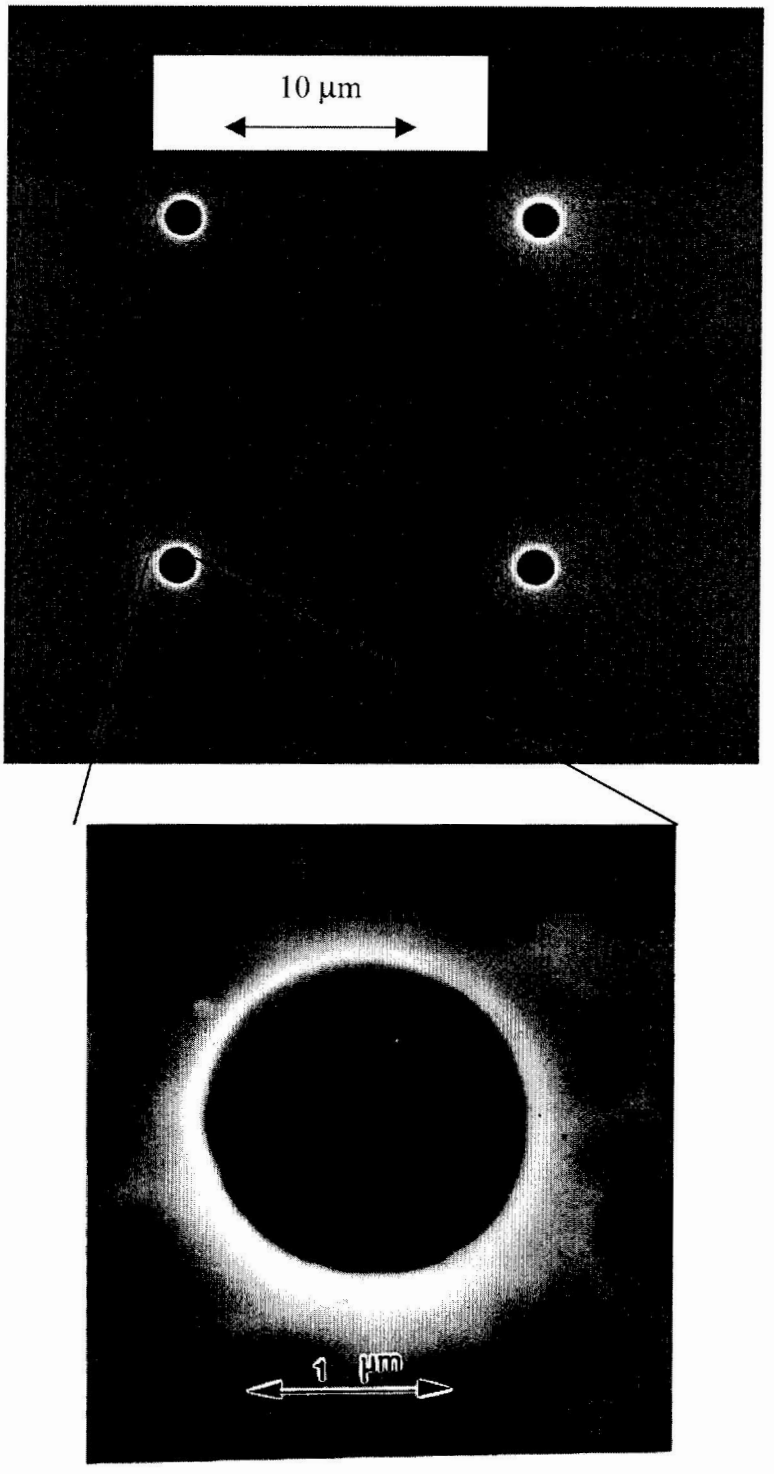

(a)

(b)

Figure 5.2 SEM microphotography of finished gated photocathodes.

A buffered HF, known for good etching selectivity, was used to etch the SiO in holes to undercut up to 0.5 μm below the top chromium layer. The undercut space guarantees the gate and cathode are not shorted when the gold film is deposited as a last step. The undercut space also reduces the space charge effect caused by the electrons on the insulator surface.

Finally, a 10-15 nm thick gold film, which forms the photocathode, was deposited to overlap the cathode metal. A tungsten basket was used to heat gold wire (0.2 mm in diameter). The gold film was deposited at ~1100 °C (melting point, 1063 °C) with a deposition speed of ~2 Å/s.

Thus a well-defined, self-aligned, micrometer scale thin-film gated photocathode was fabricated. The scanning electron microscopy (SEM) micro-photographs of a finished photocathode are shown in Figure 5.2a and 5.2b. The fabrication process used here was developed for the available equipment. The practical gated photocathodes would be fabricated by conventional semiconductor processes which will be described in Chapter 6.

5.2 Experimental I-V characteristics

There are three current components, the cathode current: I_c, the gate current, I_g, and the anode current (or beam current), I_a. For an ideal case, I_c is equal to the sum of I_g and I_a. These currents depend on the electrical field between anode and gate, the gate voltage, and the dimensions of the gated photocathode. Ten samples with different configurations, as listed in Table 1, have been characterized.

Table 5.1 List of samples: d = gate diameter, t = insulation layer thickness, t' = gate metal thickness

#	1	2	3	4	5	6	7	8	9	10
d (μm)	2.4	2.5	2.4	1.7	2.4	2.8	2.9	2.0	2.4	2.9
t (μm)	1.7	1.45	1.4	1.4	2.3	2.3	2.3	1.45	1.45	1.45
t' (nm)	90	90	85	98	90	120	80	100	100	100

The gated photocathodes were mounted on a stage, the cathode was grounded and the gate was biased from –2 volts to 15 volts. An anode was set parallel to the cathode with a separation of 0.7 mm, and an accelerating field was established between the anode and the gated photocathodes by applying a positive voltage on the anode. A 257 nm laser illuminated the photocathode from the backside (transmission model). The currents were measured as a function of gate voltage, V_g, for different accelerating fields, E_2, using a lock-in amplifier [3]. The chopper frequency was set at 30 Hz to reduce any signal loss through the conducting cable.

As described in Chapter 4, when the gate voltage is below the extinction gate voltage, V_x, the emission current is turned off. During the actual experimental set up, however, this was not the case. Measurable and approximately equal anode and gate currents were detected even when there was no measurable cathode current. The anode and gate currents, in this instance, are attributed to spurious photoemission currents from the gate metal due to the reflected light from the anode. Because the field between the anode and the gate, E_2, remains nearly unchanged for the I-V measurement, the spurious currents were assumed to be constant and were subtracted from the measured currents to obtain the real I-V characteristics.

5.3 Calibrating the quantum yield of thin-film gated photocathodes

The I-V characteristics of a thin-film gated photocathode are a function of both its photoemission properties and dimensions. The quantum yield of a photocathode is known to be strongly dependent upon the thickness and the surface chemical state [5,6]. The currents can vary significantly from one photocathode to the other. It is thus desirable to leave out the effect of quantum yield of the photocathodes, and obtain the dimension and the electric field effects only. This can be realized by normalizing the I-V curves. The photocurrent, measured from the parallel plane electrodes with small separation, becomes saturated once the anode voltage is positive with respect to that of the cathode. Because the anode collects all of the emitted electrons in every energy level and in every direction, as expressed in Equation (4.3). For the low current density (<1000 A/cm^2) as in this study, the space charge is insignificant and the photocurrent keeps saturated until the field is high enough to introduce the Schottky effect. Thus the saturation current measured/calculated in a low field (< 1 V/μm) can be used to perform the normalization. Theoretically, as described in Chapter 4, the current can be normalized by divided by the saturated photocurrent from the same photoemission area, without the Schottky effect.

Experimentally, this can be done by calibrating the quantum efficiency. The calibration was done using a photocathode without the gate structure but with the same photoemission area as that of the gated photocathodes. The conducting metal stack of 100 nm Cr and 200 nm Au was thick enough to block the photoemission, except in the photoemission area, but not too thick as to catch the high solid angle photoemission from the defined area. The calibrating photocathodes were fabricated by the same process as the gated photocathode in order to have the same quantum yield. The same photon energy was used to measure the currents from the gated photocathode and the calibrating photocathode. The saturation current of the calibrating photocathode was measured under a low field to avoid the Schottky effect. The currents measured from

gated photocathodes divided by this saturation current can be regarded as the equivalent of theoretically normalized currents.

The normalized currents don't depend on the quantum yield of the photocathode and therefore it allows the comparison of gated photocathodes with a range of quantum yield. It also allows the comparison of I-V characteristics of gated photocathodes with different gate diameter.

5.4 Results and discussion

In this section all of the factors affecting the I-V curve are discussed, including accelerating field, E_2, gate voltage, V_g, gate diameter, d, insulator thickness, t, and gate metal thickness, t'. Of these parameters, E_2 and d are major factors to determine the extinction gate voltage, the ratio of d/t determines the slope in region II, and t determines the slope in region III.

Figure 5.3 shows the normalized I-V curves from a gated photocathode with d = 2.4 μm, t = 2.3 μm and E_2 = 0.1 V/μm. The experimental results were compared with the theoretical ones. As predicted in Chapter 4, three regions are clearly defined. In region I, the gate voltage is beyond a negative gate voltage, V_x, and the cathode current is zero. In region II and III, the gate voltage is larger than V_x; the cathode current increases as the gate voltage increases. The slope in region II is due to the energy spread of the photoemission, and the slope in region III is due to the work function lowering. The anode current has a similar trend to the cathode current. The gate current is small compared with the beam current for a low gate voltage but becomes larger with increases in the gate voltage. The measured currents were in excellent agreement with the theoretical predictions except for light degrees of deviation between the measured gate and the anode currents for a high gate voltage region. This deviation is caused by the thickness of the gate metal and will be discussed later.

Figure 5.4a shows I-V curves from a gated photocathode with d =1.7 μm and t = 1.4 μm for E_2 = 0.1 and 0.4 V/μm. The currents depend on E_2 but the difference is too small to differentiate. This effect was simulated as shown in Figure 5.4b. Limited by the experiment conditions, the I-V curves are measured with a range of E_2 from 0.1 to 0.4 V/μm. Hereafter, all of the I-V curves were measured with E_2 = 0.1 V/μm.

Figure 5.5a shows the effect of the gate diameter for a constant insulator thickness and E_2 = 0.1 V/μm. Theoretical I-V curves for these configurations were also constructed (shown in Figure 5.5b). The extinction gate voltages for three cases are the same because E_2 is too small to make a difference. The slope of the cathode current in region II depends on the ratio of d/t: a bigger d/t results in a bigger slope, due to the bigger emission angles. The slopes in region III depend only on thickness and therefore are the same. The gate current is a smaller component compared with the anode current for all three configurations. The proportion of the gate current increases with a smaller gate diameter. This can be explained by the effect of fringing field created due to the gate metal thickness [7]. The fringing field, a function of gate metal thickness and gate voltage, changes electron trajectories near the gate. A positive gate voltage attracts electrons and some electrons may be collected by the gate, increasing the gate current. For a given gate metal thickness and a gate voltage, the extent of the fringing field can be regarded as a constant. The effect of the fringing field can be roughly estimated by the proportion of its extent to the gate diameter: the smaller diameter relates with a bigger proportion and therefore its effect is relatively stronger, and vice versa.

The I-V relationship to the insulator thickness for a constant gate diameter was examined from two sets of measurements: one set for d = 2.4 μm, t = 1.4 μm, 1.7 μm, and 2.3 μm, is shown in Figure 5.6a and compared with the simulation of Figure 5.6b. The other set for d = 2.9 μm, t = 1.45 μm and 2.3 μm, is shown in Figure 5.6c and compared with the simulation shown in Figure 5.6d. The extinction gate voltage weakly depends on the insulation layer thickness for a given gate diameter and accelerating field. The slope of the cathode current in region II depends on the d/t ratio, as described

above. The slope and magnitude of I-V curves in region III depends on the thickness of the insulator: the thinner insulator results in a bigger slope. This effect has been ascribed to the Schottky effect as explained in Chapter 4. The gate currents are again smaller than the anode currents. The ratio of the anode current to the cathode current, or the efficiency of the gated photocathode, is almost the same for the two sets respectively. This is due to the same reason as describe in previous paragraph - the extent of the fringing field is the almost same for the same gate diameter.

The gate metal thickness has a great impact on the operation of the thin-film gated photocathodes. As mentioned above, the fringing field around the gate edge is a function of the gate metal thickness. For the thicker (> 90 nm) gate metal, with a high gate voltage, the fringing field is strong and more electrons are trapped. For the thin gate metal, however, the lateral field is limited to a small region even for high gate voltage. The gate metal thickness in this study ranges from 80 nm to 120 nm. For most gated photocathodes with a gate metal thickness of less than 90 nm, the gate current is about 5% of the cathode current for a small gate voltage (< 5 volts) and up to 20% or more for a bigger gate voltage (> 10 volts). An extreme case was found in sample 6, as shown in Figure 5.7, with d = 2.8 μm, t = 2.1 μm and t' = 120 nm, in which the gate current exceeds the anode current.

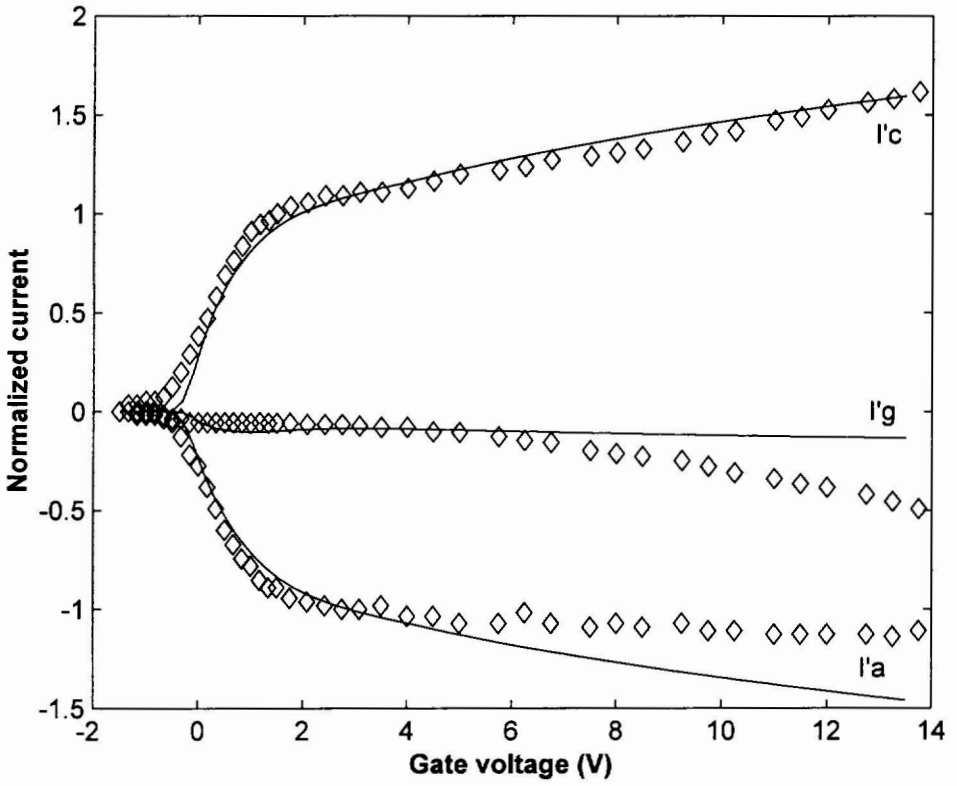

Figure 5.3 Measured I-V curves of a gated photocathode with d = 2.4 μm, t = 2.3 μm and E_2 = 0.1 V/μm, compared with the simulation results.

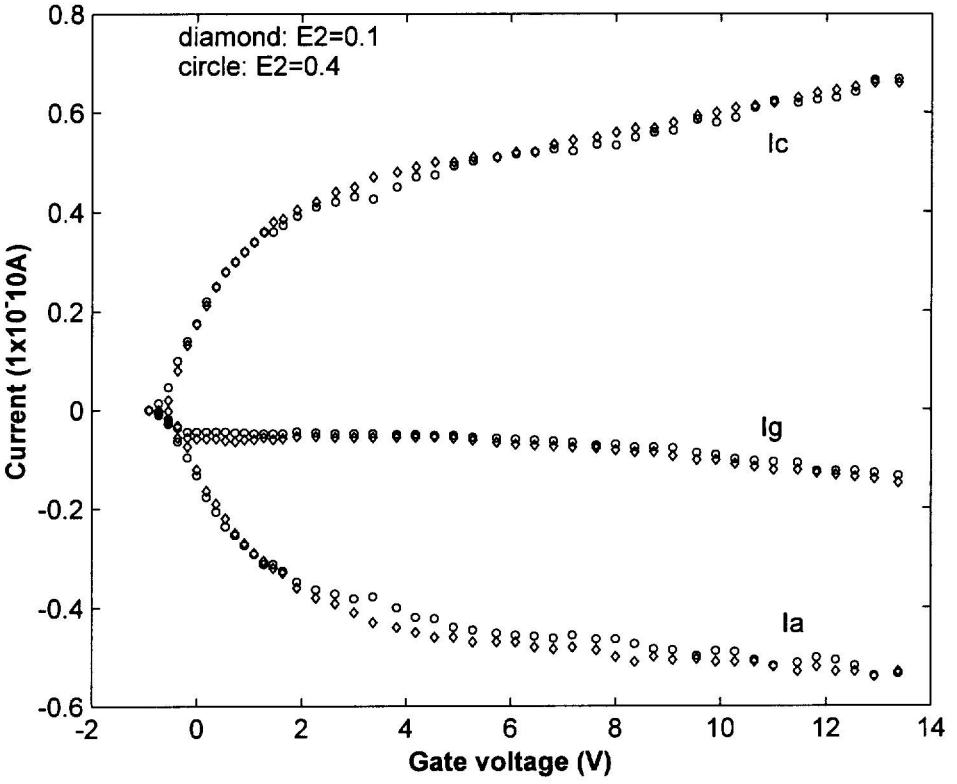

Figure 5.4a Measured I-V curves of a gated photocathode with d = 1.7μm and t = 1.4 μm for E_2 = 0.1 and 0.4 V/μm.

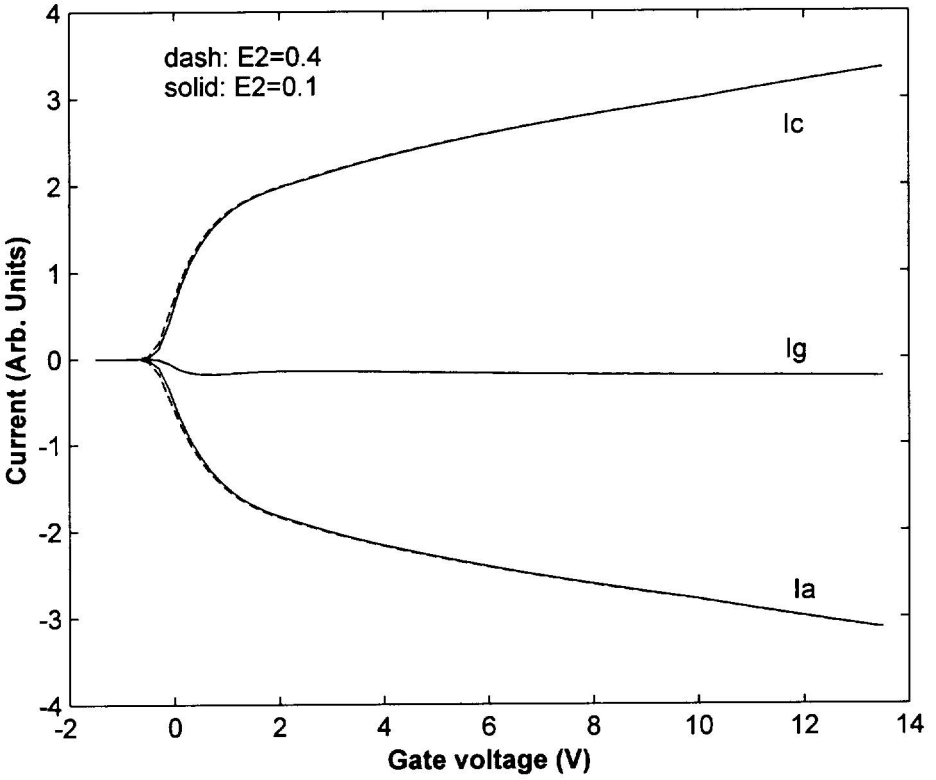

Figure 5.4b Simulated I-V curves of a gated photocathode with d = 1.7μm and t = 1.4 μm for E_2 = 0.1 and 0.4 V/μm.

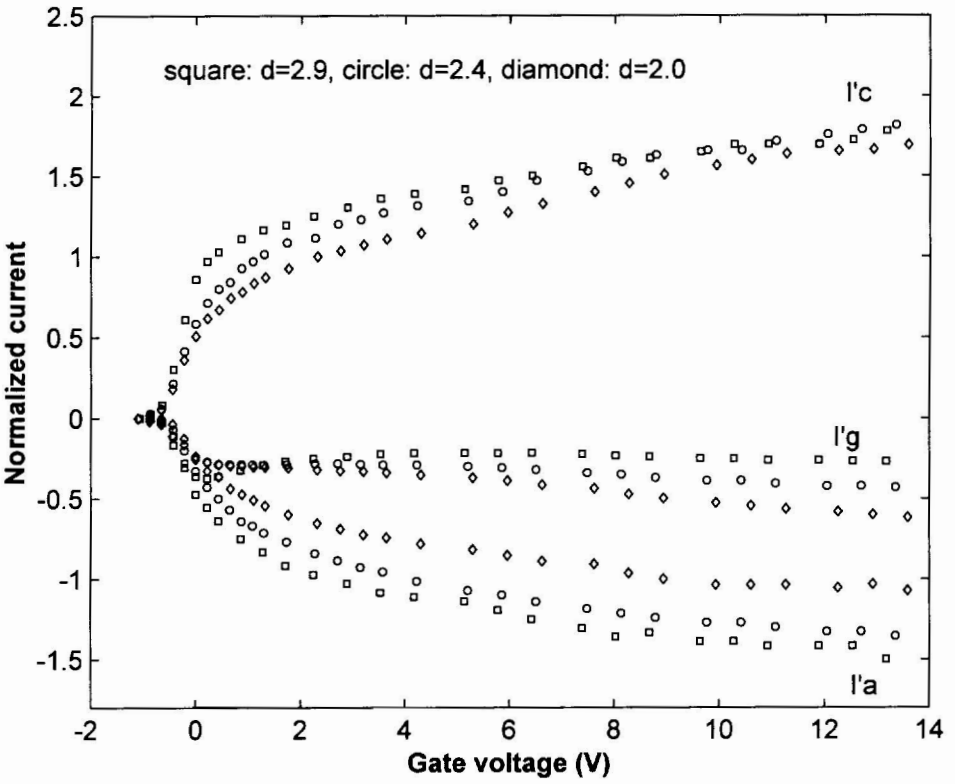

Figure 5.5a Measured I-V curves showing the effect of gate diameter (d = 2.0 2.4 and 2.9 μm) for a constant insulator thickness, t = 1.45 μm and E_2 = 0.1 V/μm.

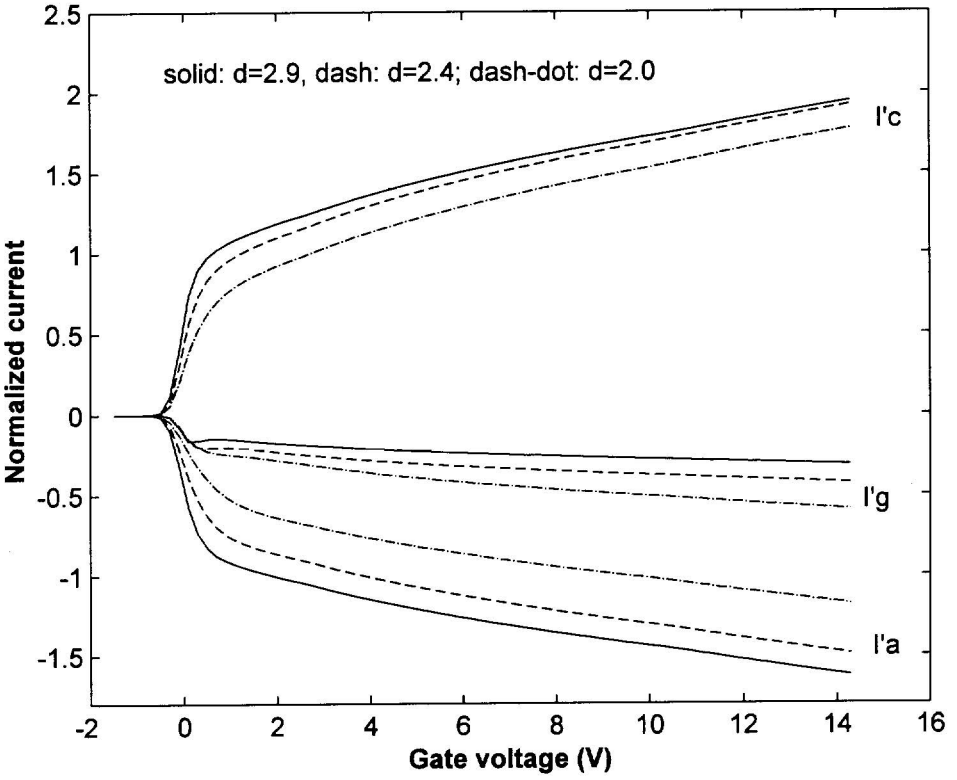

Figure 5.5b Simulated I-V curves showing the effect of gate diameter (d = 2.0 2.4 and 2.9 μm) for a constant insulator thickness, t = 1.45 μm and E_2 = 0.1 V/μm.

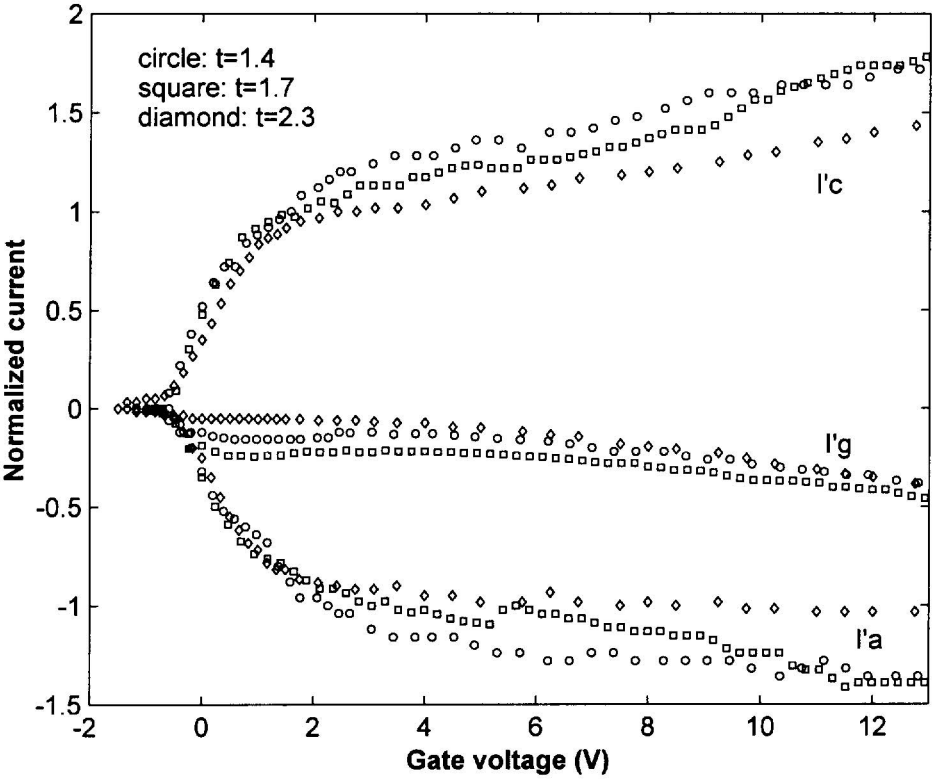

Figure 5.6a Measured I-V curves for a constant gate diameter (d = 2.4 μm) showing the effect of insulator thickness (t = 1.4, 1.7 and 2.3 μm) with E_2 = 0.1 V/μm.

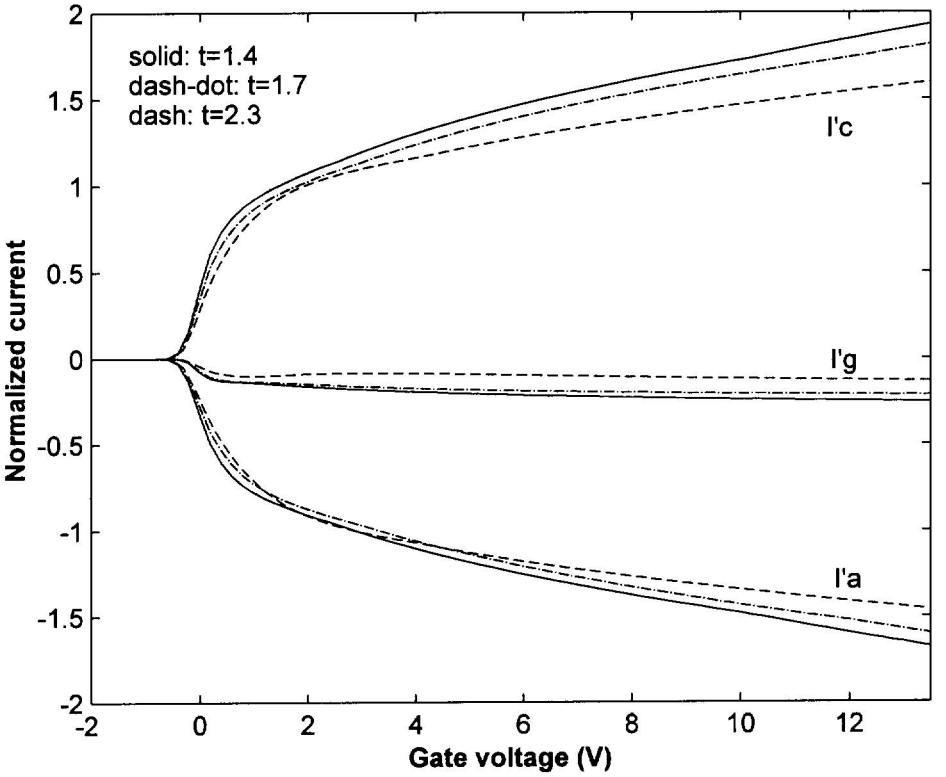

Figure 5.6b Simulated I-V curves for a constant gate diameter (d = 2.4 μm) showing the effect of insulator thickness (t = 1.4, 1.7 and 2.3 μm) with E_2=0.1 V/μm.

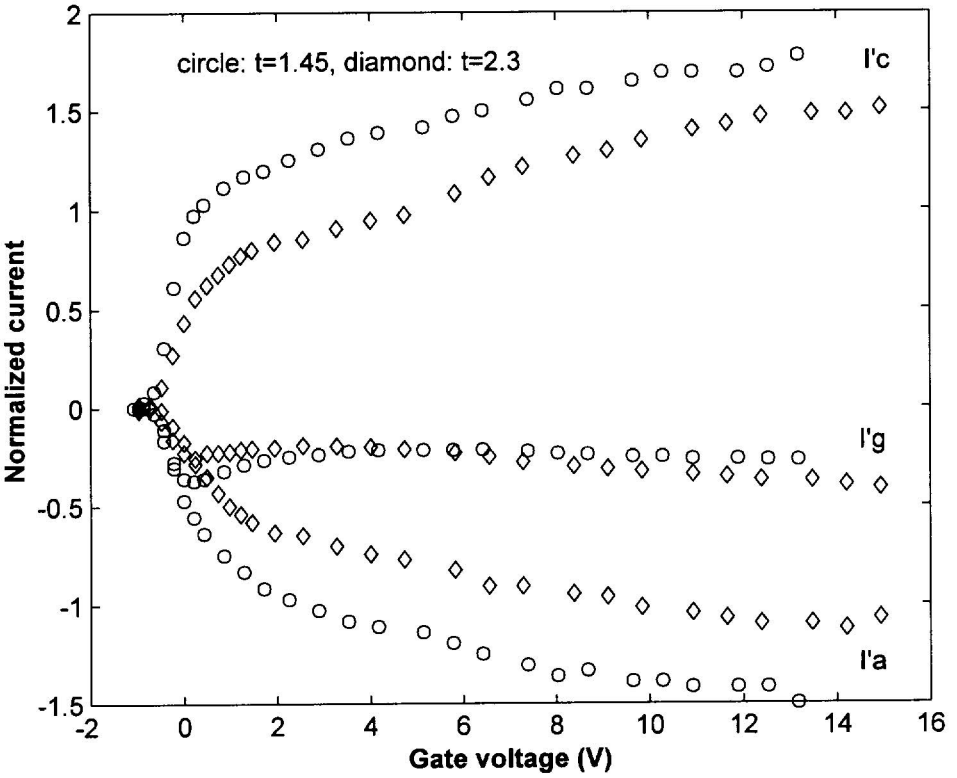

Figure 5.6c Measured I-V curves for a constant gate diameter (d = 2.9 μm) showing the effect of insulator thickness (t=1.45 and 2.3 μm) with E_2=0.1 V/μm.

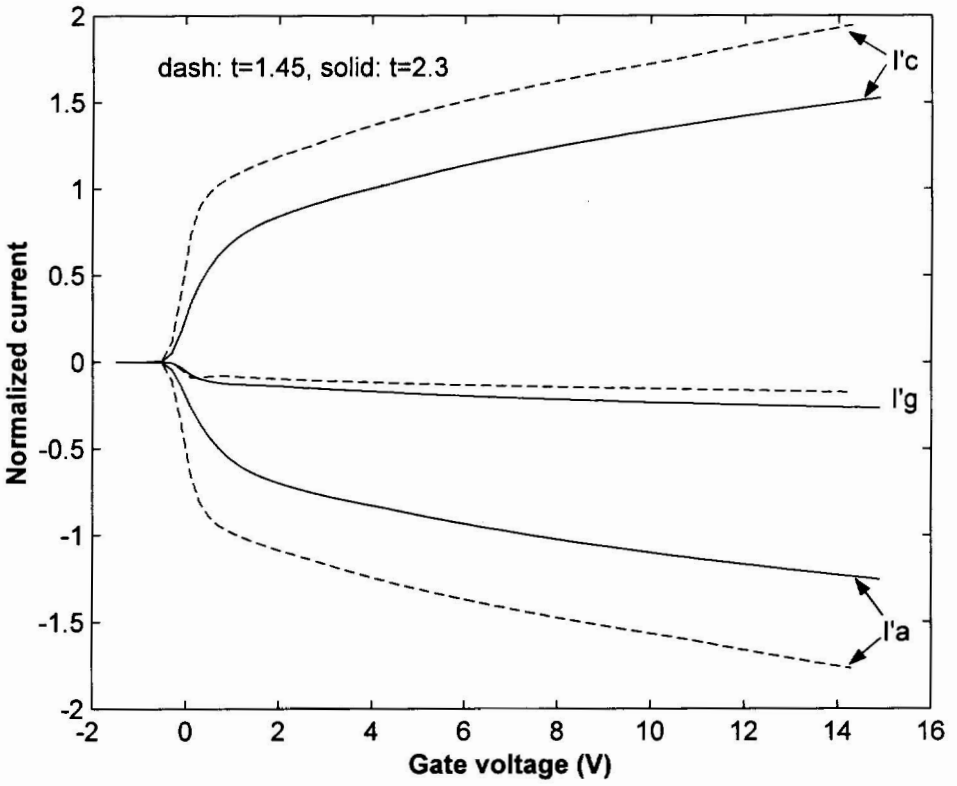

Figure 5.6d Simulated I-V curves for a constant gate diameter (d = 2.9 μm) showing the effect of insulator thickness (t = 1.45, 2.3 μm) with E_2=0.1 V/μm.

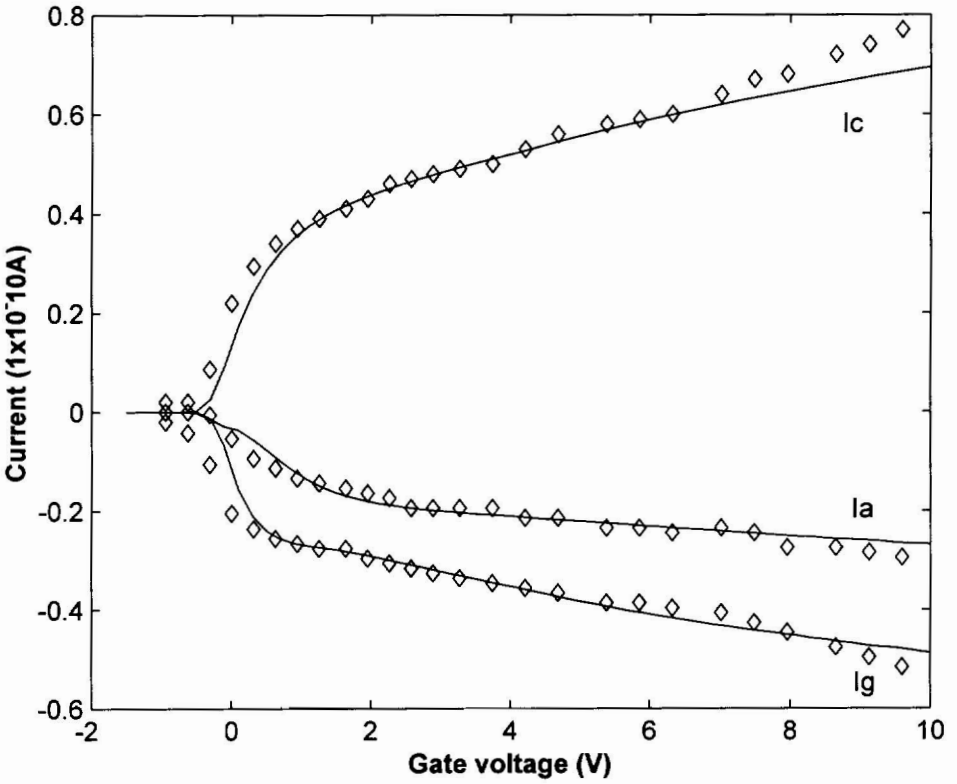

Figure 5.7 I-V curves of a gated photocathode with d = 2.8 μm, t = 2.1 μm and a thick gate metal of t' = 120 nm, for E_2 = 0.1 V/μm. The gate current exceeds the anode current.

Summary

Thin-film gated photocathodes with different geometric configurations were successfully fabricated. The current-voltage characteristics from these devices have been fully explored, are well defined and are consistent with theoretical expectations. Three regions of I-V curve have been defined.

The studied structures were turned off by applying a negative voltage of several volts to the gate. The extinction gate voltage was found to be a strong function of the gate diameter and the accelerating field.

The insulation layer thickness was found to play a critical role in the operation of the thin-film gated photocathodes. The beam current was enhanced by the high electric field created by a thin insulator and a high gate voltage.

Photoemission from the cathode can be efficiently delivered from the gated structure, and only a small portion of electrons were collected by the gate. An extreme thin metal film gate effectively limits the gate current, by which the efficiency of a thin-film gated photocathode is improved.

With these studies, the concept of the thin-film gated photocathode was proved and the theory has been verified. Thin-film gated photocathodes are expected to be a feasible approach to multiple-beam electron-beam lithography.

References

[1] J. Melngailis, "Critical review, fucosed ion beam technology and applications," J. Vac. Sci. Technol. B **5**, pp. 469-495, 1987.

[2] A. L. Shabalov and M. S. Feldman, "Optical and dielectric properties of thin SiO_x films of variable composition," Thin Solid Films, **110**, pp. 215-224, 1983.

[3] W. E. Spicer, "Photoelectric emission," in Optical Properties of Solids, Ed. By F. Abeles, North-Holland Publishing Company, p. 755, 1972.

[4] Z. Pei, J. McCarthy, C. N. Berglund, T. H. P. Chang, M. Mankos, K. Y. Lee and M. L. Yu, "Thin-film gated photocathodes for electron-beam lithography," J. Vac. Sci. Technol. B **17**, pp. 2814-2818, 1999.

[5] X. Jiang, C. N. Berglund, A. E. Bell, and W. A. Mackie, "Photoemission from gold thin films for application in multiphotocathode arrays for electron beam lithography," J. Vac. Sci. Technol. B **16**, pp. 3374-3379, 1998.

[6] S. Gosavi et al. "Practical gold thin-film photocathodes for advanced electron beam lithography," Symposium on Photomask Technology, Proceedings of SPIE, Vol. 3837, Monterey, CA, September, pp. 501-512, 1999.

[7] G. Liebmann, "The electrostatic field distribution near a circular aperture or short cylinder," Phil. Mag. **39**, pp. 281-296, 1948.

Chapter 6
Practical Thin-Film Gated Photocathodes: Proposed Configuration of Thin-Film Gated Photocathode Arrays and Fabrication Processes

The work so far has demonstrated the feasibility of thin-film gated photocathodes, addressed some of the operational principles and studied in detail the I-V characteristics experimentally and theoretically. For practical applications, however, two issues have not been addressed: the structure and the operating conditions of an actual thin-film gated photocathode array and the fabrication process. These issues are examined in this chapter. An addressable gated photocathode array with a controlling gate is first proposed, an example of the fabrication processes for such a device is then discussed.

6.1 Addressable thin-film gated photocathodes arrays

It has been mentioned in Chapter 1 and Chapter 2 that, for the multiple-beam, maskless, direct writing, electron-beam lithography system, the beams need to be independently modulated. For the case of gated photocathodes, individually modulating the electron beams requires the application of different voltages on each individual gate. This structure is called an addressable thin-film gated photocathodes array.

The addressable array of electron sources has been reported for a field emission source [1] and negative electron affinity (NEA) photocathode source [2]. For the field

emission case, as the device was fabricated on a Si wafer, an integrated CMOS circuit addressed and controlled the electron-beams. For the NEA photocathode case, a controlling gate with a negative bias with respect to the cathode addresses the electron-beams and is quite similar to the structure studied in this thesis.

As mentioned in Chapter 1, the thin-film gated photocathodes will be integrated into a multisource system which uses one set of optics. Due to the constraint of off-axis aberrations, the maximum array size has to be limited to approximately 300-400 μm in diameter [3]. To increase the number of the beams, the center-to-center spacing between the beams has to be reduced. When the spacing is less than a certain point, the interbeam interaction will result in beams blurring in the system. For example, for a 10 nA beamlet, the spacing is around 30 μm to obtain the smallest spot size at the wafer surface [4,5].

For metallic photocathodes, the beam current might be lower than 10 nA [3], and the beam pitch can be less than 30 μm. Problems, however, might arise for the addressable array for this spacing: (1) The extinction gate voltage of one gated photocathode will be higher due to the high potential neighboring gates; (2) The shape of the electron beam from one gated photocathode will be distorted due to the low potential neighboring gates. To solve these problems, we propose the structure shown in Figure 6.1: a shielding electrode built on top of the controlling gate with a separation distance of approximately the spacing between the gate and the cathode. The diameter of the shielding electrode should be 1.2~1.5 times bigger than that of the controlling gate.

If the shield electrode is grounded (with a grounded cathode), it can effectively block the interference [2,6]. The shielding gate can also affect the shape of the beam, which can be inferred from the studies of the field emission displays (FED) [7-10]. For the structure used in FEDs, two gates are used, a high positive (~100 volts) voltage is applied to the lower gate to form the strong electric field necessary for field emission, while the upper gate is negatively biased from 0 to several volts to focus the beams. The upper gate is equivalent to the shield electrode in this study.

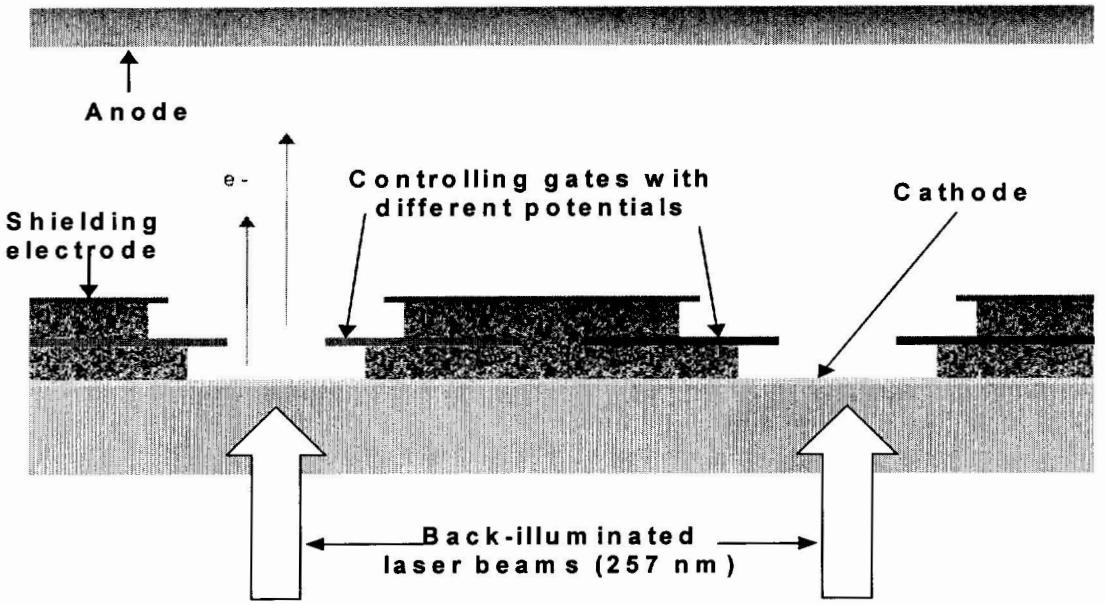

Figure 6.1a Cross-sectional diagram of an addressable gated photocathode array (with the shielding electrode and the cathode grounded).

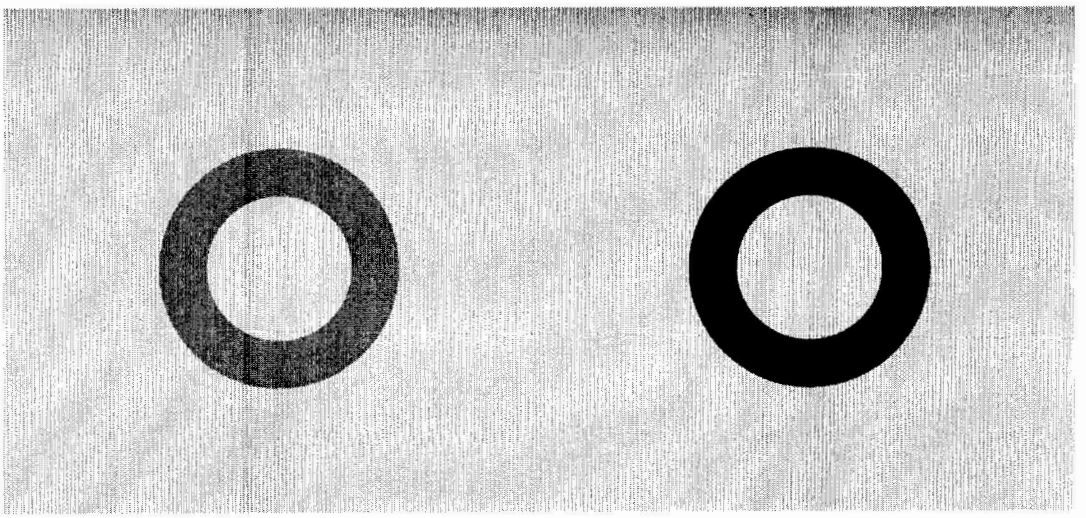

Figure 6.1b Top view of an addressable gated photocathode array.

For practical applications, the thin-film gated photocathode array should be able to provide switching in the hundreds of mega Hertz frequency range for modulation of the electron beams. The operational frequency can be estimated by checking the array circuit model. If the substrate is 30 mm in diameter, with a gate metal width of 50 μm, an insulation layer of SiO_2 with a thickness of 0.5 μm, the total capacitance is only $1x10^{-10}$ F. Even if the total resistance is several Ohms, the operation frequency is still in the giga Hertz range. If an application specified integrated circuit (ASIC) is integrated with the array to be used as an array driver, the operation frequency will be limited by the speed of the ASIC.

6.2 Fabrication processes

The device described in figure 6.1 can be fabricated by conventional silicon processing technology. There are at least two ways to build such a structure [11]. First, using silicon-on-sapphire, the active electronic driver array and all the interconnections are fabricated using conventional silicon integrated circuit fabrication techniques, and the structures (as shown in Figure 6.1) are constructed after the silicon layer is removed. Second, using a silicon wafer to fabricate the electronic drive array, holes are etched through the silicon wafer where gated photocathodes are to be constructed. In the following section, the first approach will be used as an example to address the fundamental processing issues.

There are various materials and processes used to fabricate such a device. Choice of materials and processing, however, has several constraints. First, the device should be physically stable. To build stable devices, stress should be minimized. There are basically two kinds of stress related to the thin-film structures: intrinsic stress and extrinsic stress. The former arises from the fabrication process in which different films are deposited at elevated temperatures and upon cooling the difference of coefficient of thermal expansion (CTE) of different materials results in residual compression/tensile

stress in the device. The later arises when the device works at an elevated temperature condition, and the stress is produced as a result of the different CTEs of different materials. Lower temperature processing (<450 °C) is favorable to limit the intrinsic stress. The materials with similar CTE will limit both intrinsic and extrinsic stress. Also the materials should bond to each other and withstand stresses that develop during normal temperature cycling or service.

Secondly, the beam variation should be limited to around 5%. It has been shown that the quantum yield of a thin-film is very sensitive to its thickness [12]. To obtain a uniform beam brightness or intensity, the thickness of the photocathode materials has to be uniform. Fortunately, present film deposition technology has a very good thickness control, with only a slight percent of variation across a diameter of 200 mm.

Thirdly, the process should be cost effective. As much as possible a Si-standard process should be used.

In this study, a gold thin-film was used as the photocathode material and it is assumed that gold will be used for future gated photocathodes. The discussion that follows is based on this assumption.

The substrate should have good optical and thermal conductivities. There are two candidates for the substrate: sapphire and fused silicon. The sapphire is favored in terms of thermal conductivity. The substrate should not react with the photocathode either.

For the cathode metal, its resistance is the major concern. The cathode metal should have a low resistance. For a big array of photocathodes and high cathode current the voltage drop on the cathode metal may impact the operational uniformity of the array. In this regard, gold is a good candidate for the cathode metal with a resistance of several mΩs. Another advantage of using gold is the zero contact potential. Gold, however, has a bad adhesion to both the substrate and insulator. Additional adhesive layers are needed to "glue" the gold film to the substrate and the insulator. Ti and Pt are ideal for such an application.

As discussed in Chapter 4 and 5, the gate metal thickness should be minimized, as long as mechanical stability is achieved. Refractory materials such as Ti, Pt, and W may be used.

The insulation materials should be chosen to sustain a high electric field for a high current electron beam. SiO_2 and Si_3N_4 are two candidates.

The metal films can be deposited by sputtering, and dielectric materials can be deposited by chemical vapor deposition (CVD) process [13]. The dry etching process is recommended for all metal layer and dielectric layer etching. These processes are low temperature, standard silicon processes.

References

[1] V. I. Merkulov, et al. "An addressable field emission array for e-beam lithography using planar, pulsed-laser deposited amorphous diamond cathodes," Proceedings of the IEEE International Vacuum Microelectronics Conference, Jul. 19-24, Asheville, NC, pp. 178-179, 1998; M. J. Paulus, et al., "Addressable amorphous diamond field emission array for e-beam lithography," Annual Device Research Conference Digest Proceedings of the 1998, Jun. 22-24, Charlottesville, VA, pp. 122-123, 1998.

[2] E. J. P. Santos and M. C. MacDonald, "Integration of microstructures onto negative electron affinity cathodes: Fabrication and operation of an addressable negative electron affinity cathode," J. Vac. Sci. Technol. B **11**, pp. 2362-2366, 1993.

[3] M. Mankos, S. Coyle, A. Fernandez, A. Sagle, P. Allen, W. Owens, J. Sullivan and T. H. P. Chang, "Multisource optimization of a column for electron lithography," J. Vac. Sci. Technol. B **18**, pp. 3010-3106, 2000.

[4] J. E. Schneider, et al, "Semiconductor on glass photocathodes as high-performance sources for parallel electron beam lithography," J. Vac. Sci. Technol. B **14**, pp. 3782-3786, 1996.

[5] J. E. Schneider, et al, "Patterned negative electron affinity photocathodes for maskless electron beam lithography," J. Vac. Sci. Technol. B **16**, pp. 3192-3196, 1998.

[6] P. Kruit, "High throughput electron lithography with the multiple aperture pixel by pixel enhancement of resolution concept," J. Vac. Sci. Technol. B **16**, pp. 3177-3180, 1998.

[7] W. D. Kesling and C. E. Hunt, "Beam focusing for field-emission flat panel displays," IEEE Transactions on Electron Devices, **42**, pp. 340-346, 1995.

[8] C. Py, J. Itoh, T. Hirano, and S. Kanemaru, "Beam focusing characteristics of silicon microtips with an in-plane lens," IEEE Transactions on Electron Devices, **44**, pp. 498-502, 1997.

[9] T. Ko, B. Chung, J. Y. Lee, and D. Jeon, "Fabrication and simulation of a gated thin film emitter," J. Vac. Sci. Technol. B **16**, pp. 700-704, 1998.

[10] Y. Toma, S. Kanemaru, and J. Itoh, "Electron-beam characteristics of double-gated Si field emitter arrays," J. Vac. Sci. Technol. B **14**, pp. 1902-1905, 1996.

[11] C. Neil Berglund, 1999 Annual report: system-level and architectural considerations of multi-electron-beam lithography, Etec Systems, Inc., Hayward, CA..

[12] X. Jiang, et al. "Photoemission from gold thin films for application in multiphotocathode arrays for electron beam lithography," J. Vac. Sci. Technol. B **16**, pp. 3374-3379, 1998.

[13] For example, D. Widmann, H. Mader, and H. Friedrich, Technology of Integrated Circuits, Springer, New York, 2000.

Chapter 7
Summary and conclusions

Thin-film gated photocathodes offer an attractive option for use in multiple-beam electron-beam lithography. The objective of this research was to prove the feasibility of the thin-film gated photocathode and to characterize its I-V relations. Major contributions of this dissertation include both theoretical modeling and experimental results, which demonstrated the practical potential of these devices.

The feasibility was first proved by turning off the emission. Electrical switching off the electron-beam by applying a negative voltage on the gate with respect to the cathode is one of the most important advantages of the thin-film gated photocathode over the conventional photocathodes. By analyzing the electric field of such devices and the photoemission properties of thin-film photocathodes, the extinction gate voltages were calculated for a variety conditions and found that only several volts are needed to turn off the electron beam. Thin-film gated photocathodes were fabricated to demonstrate this concept. Extinction gate voltages were measured from these structures and a good agreement with calculation was obtained.

I-V characteristics were then studied experimentally. Different device fabrication schemes were examined, and once a successful scheme was demonstrated ten different gated photocathodes with different geometric configurations were fabricated. The current as a function of gate voltage was measured for these devices subjected to a range of electric fields. A typical I-V characteristic was reproduced, in ten gated photocathodes, showing three clearly defined regions: in region I, currents are zero when the gate voltage lower than the negative extinction gate voltage; in region II,

the cathode and the anode current increase with gate voltage. The gate current is constant and smaller than the anode current. In region III, all of the currents increase with gate voltage with a finite slope. The effects of the gate diameter, the insulation layer thickness, the gate metal thickness and accelerating field on these parameters have also been examined during the course of this research.

The principles of operation of the thin-film gated photocathode have been explored by analyzing the electric fields and photoemission properties of the photocathode. The energy distribution curve (EDC) and angular distribution curve (ADC) for a gold thin-film have been modeled using the three-step model. Experimental measurements were carried out to verify the theoretical model. I-V characteristics of thin-film gated photocathodes were calculated by using theoretical EDC, ADC and ray tracing methods. By incorporating the Schottky effect, the model successfully simulated the I-V characteristics and the related parameters of the gate voltage, the accelerating field and the dimensions of the gated photocathode.

One important method used in I-V characterization is that the currents are normalized, i.e. the currents divided by the saturation current measured at a low field from the same photoemission area. The normalized current does not depend on the quantum yield of the photocathode. The significance of the normalized current is triple fold: (1) It allows the comparison of I-V characteristics of gated photocathodes with different photocathode diameter; (2) It eliminates the quantum yield variations from one gated photocathode to the other, and therefore it allows the comparison of gated photocathodes with a range of quantum yield; and (3) It allows the prediction of current magnitude for a given gated photocathode structure with a known quantum yield for the emitting thin film.

The experimental results of I-V characteristics were in excellent agreement with theoretical analysis, and the validity of the assumptions and methods used in this dissertation are thus justified. The general behavior of thin-film gated photocathodes was quite predictable and consistent with the expectations. The models not only

explained the operational principles of the thin-film gated photocathodes but also provide an insight into the emission process of gated photocathodes.

Perhaps the most significant discovery was the finite slope in region III of the I-V curve was explained by the Schottky effect. The Schottky effect predicts that a higher beam current is obtainable by using a combination of thin insulation layer and high gate voltage with the insulation layer thickness as a dominant factor.

The other significant discovery was the effect of gate metal thickness on the I-V relation: a thin gate results in a smaller gate current and therefore a higher ratio of the anode current to the cathode current, a higher emission efficiency. This discovery suggests that the gate metal should be as thin as possible as long as the gate metal has enough mechanical strength.

Although an array of gated photocathodes has been proposed and some issues have been addressed in Chapter 6, several practical issues need to be examined. The first is to study the brightness of the gated photocathodes. The brightness is an important parameter of the electron source because it controls the throughput of an EBL system. For a given gated photocathode, the brightness is a function of the controlling gate voltage, the shielding electrode voltage and the accelerating field. To study the brightness of the gated photocathodes, a Delong chamber with a faraday cup may be used. The brightness can be measured indirectly by measuring the spot size and intensity profile of the image on the phosphorus screen.

The second issue to pursue further is to optimize the structure and voltages of the array to minimize the interaction between the beams. The shielding electrode was proposed to block the interaction. The diameter of the holes on the shielding gate and the center-to-center distance of the holes need to be optimized. The optimization can be done by both simulation program and experiment. A Delong chamber may also be used.

Finally, the switching frequency range needs to be explored. In Chapter 6, the driving circuit was proposed to be the limiting factor of the switching frequency. Independent experimental study is needed to verify this assumption and measure the actual operation range.

In conclusion, the thin-film gated photocathode allows the currents from the photocathode to be electrically modulated, or switched on and off, by applying only a few volts to the gate. This feature reduces the complexity, improves the reliability, provides the flexibility and adds efficiency to the whole lithography system. Due to the use of a thin insulation layer and a thin gate, the thin-film gated photocathode is able to deliver higher beam current, better defined electron-beams than the conventional photocathodes. Thin-film gated photocathodes may offer an attractive option for use in multiple-beam electron-beam lithography.

VITA

Zeting Pei was born in Shanxi, China on July 23, 1966. He attended the Central-South University of Technology in Changsha, China, and received the degree Bachelor of Science in Materials Science and Engineering in July 1989. Subsequently, he took several engineer positions in metallurgy industry.

In September 1996, he began his graduate studies at the Oregon Graduate Institute of Science and Technology. He received the degree Master of Science in Materials Science and Engineering in April 1998. He then switched to the Department of Electrical and Computer Engineering at the same institute to pursue his Ph.D. in Electrical Engineering. He completed all requirements for the degree Doctor of Philosophy in Electrical Engineering in February 2001.

His research interests include solid-state device, electronic materials, and semiconductor processing. He has authored several scientific publications during the years at OGI.

He is leaving to accept a position of product engineer at SDL, Inc., San Jose, California.